



1 **FTIR time series of tropospheric HCN in eastern China:**
2 **seasonality, interannual variability and source attribution**

3 Youwen Sun ¹⁾, Cheng Liu ^{1, 2, 3, 4, 5)*}, Lin Zhang ^{6)*}, Mathias Palm ⁷⁾, Justus Notholt ⁷⁾, Hao Yin ¹⁾,
4 Corinne Vigouroux ⁸⁾, Erik Lutsch ⁹⁾, Wei Wang ¹⁾, Changong Shan ¹⁾, Thomas Blumenstock ¹⁰⁾,
5 Tomoo Nagahama ¹¹⁾, Isamu Morino ¹²⁾, Emmanuel Mahieu ¹³⁾, Kimberly Strong ⁹⁾, Bavo Langerock
6 ⁸⁾, Martine De Maziere ⁸⁾, Qihou Hu ¹⁾, Huifang Zhang ¹⁾, Christoph Petri ⁷⁾, and Jianguo Liu ¹⁾

7 (1 *Key Laboratory of Environmental Optics and Technology, Anhui Institute of Optics and Fine*
8 *Mechanics, Chinese Academy of Sciences, Hefei 230031, China*)

9 (2 *Center for Excellence in Regional Atmospheric Environment, Institute of Urban Environment,*
10 *Chinese Academy of Sciences, Xiamen, 361021, China*)

11 (3 *University of Science and Technology of China, Hefei, 230026, China*)

12 (4 *Key Laboratory of Precision Scientific Instrumentation of Anhui Higher Education Institutes,*
13 *University of Science and Technology of China*)

14 (5 *Anhui Province Key Laboratory of Polar Environment and Global Change, USTC, Hefei,*
15 *230026, China*)

16 (6 *Department of Atmospheric & Oceanic Sciences, Peking University, Beijing, 100871, China*)

17 (7 *University of Bremen, Institute of Environmental Physics, P. O. Box 330440, 28334 Bremen,*
18 *Germany*)

19 (8 *Royal Belgian Institute for Space Aeronomy (BIRA-IASB), Brussels, Belgium*)

20 (9 *Department of Physics, University of Toronto, Toronto, Ontario, Canada*)

21 (10 *Karlsruhe Institute of Technology (KIT), Institute for Meteorology and Climate Research*
22 *(IMK-ASF), Karlsruhe, Germany*)

23 (11 *Institute for Space-Earth Environmental Research (ISEE), Nagoya University, Nagoya, 464-*
24 *8601, Japan*)

25 (12 *Satellite Observation Center, National Institute for Environmental Studies, Tsukuba, 305-8506,*
26 *Japan*)

27 (13 *Institute of Astrophysics and Geophysics, University of Liège, Belgium*)

28 Correspondence: Cheng Liu (chliu81@ustc.edu.cn) or Lin Zhang (zhanglg@pku.edu.cn)

29 **Abstract:**

30 We analyzed seasonality and interannual variability of tropospheric HCN column amounts in
31 densely populated eastern China for the first time. The results were derived from solar absorption
32 spectra recorded with ground-based high spectral resolution Fourier transform infrared (FTIR)
33 spectrometer at Hefei (117°10'E, 31°54'N) between 2015 and 2018. The tropospheric HCN columns
34 over Hefei, China showed significant seasonal variations with three monthly mean peaks throughout
35 the year. The magnitude of the tropospheric HCN column peak in May > September > December.
36 The tropospheric HCN column reached a maximum of $(9.8 \pm 0.78) \times 10^{15}$ molecules/cm² in May
37 and a minimum of $(7.16 \pm 0.75) \times 10^{15}$ molecules/cm² in November. In most cases, the tropospheric
38 HCN columns at Hefei (32°N) are higher than the FTIR observations at Ny Alesund (79°N), Kiruna
39 (68°N), Bremen (53°N), Jungfraujoch (47°N), Toronto (44°N), Rikubetsu (43°N), Izana (28°N),
40 Mauna Loa (20°N), La Reunion Maito (21°S), Lauder (45°S), and Arrival Heights (78°S) that are
41 affiliated with the Network for Detection of Atmospheric Composition Change (NDACC).
42 Enhancements of the tropospheric HCN columns were observed between September 2015 and July
43 2016 compared to the counterpart measurements in other years. The magnitude of the enhancement
44 ranges from 5 to 46% with an average of 22%. Enhancement of tropospheric HCN (Δ HCN) is
45 correlated with the coincident enhancement of tropospheric CO (Δ CO), indicating that
46 enhancements of tropospheric CO and HCN were due to the same sources. The GEOS-Chem tagged
47 CO simulation, the global fire maps and the PSCFs (Potential Source Contribution Function)
48 calculated using back trajectories revealed that the seasonal maxima in May is largely due to the
49 influence of biomass burning in South Eastern Asia (SEAS) ($41 \pm 13.1\%$), Europe and Boreal Asia



1 (EUBA) ($21 \pm 9.3\%$) and Africa (AF) ($22 \pm 4.7\%$). The seasonal maxima in September is largely
2 due to the influence of biomass burnings in EUBA ($38 \pm 11.3\%$), AF ($26 \pm 6.7\%$), SEAS ($14 \pm$
3 3.3%), and Northern America (NA) ($13.8 \pm 8.4\%$). For the seasonal maxima in December, dominant
4 contributions are from AF ($36 \pm 7.1\%$), EUBA ($21 \pm 5.2\%$), and NA ($18.7 \pm 5.2\%$). The tropospheric
5 HCN enhancement between September 2015 and July 2016 at Hefei (32°N) were attributed to an
6 elevated influence of biomass burnings in SEAS, EUBA, and Oceania (OCE) in this period.
7 Particularly, an elevated fire number in OCE in the second half of 2015 dominated the tropospheric
8 HCN enhancement in September – December 2015. An elevated fire number in SEAS in the first
9 half of 2016 dominated the tropospheric HCN enhancement in January – July 2016.

10 11 **1 Introduction**

12 Atmospheric hydrogen cyanide (HCN) is an extremely hazardous gas that threaten human
13 health and terrestrial ecosystems (Andreae and Merlet, 2001; Akagi et al., 2011; Rinsland et al.,
14 2002). Improved knowledge of the physical and chemical mechanisms which drive the observed
15 HCN variability is of great significance because HCN plays an important role in the global nitrogen
16 cycle (Andreae and Merlet, 2001; Li et al., 2003). It is well established that biomass burning is the
17 major source of tropospheric HCN and industrial emissions contribute additional minor sources of
18 HCN (Bange and Williams, 2000; Holzinger et al., 1999; Lobert et al., 1990). Li et al. (2009)
19 estimates a global source of HCN from biomass burning of $0.4 - 3.2 \text{ Tg N yr}^{-1}$ and from burning
20 domestic biofuel of 0.2 Tg N yr^{-1} (Li et al., 2009). Bertschi et al. (2003) estimates a global fossil
21 fuel combustion source of $0.04 \text{ Tg N yr}^{-1}$, negligibly small in comparison (Bertschi et al., 2003).
22 The principle pathway for HCN sink is ocean uptake which accounts for 0.73 to 1.0 Tg N/year (Li
23 et al., 2009). Additional minor sinks of HCN are attributed to atmospheric reaction with hydroxyl
24 radical (OH) and O^1D , and photolysis (Li et al., 2000; Nagahama and Suzuki, 2007). The life time
25 of HCN is 2 – 5 months in the troposphere and several years in the stratosphere. Li et al. (2003,
26 2009), Lupu et al. (2009), Vigouroux et al. (2012), and Zeng et al. (2012) showed that the observed
27 variability of HCN can be reproduced by the chemical model simulations where biomass burning
28 and ocean uptake provide the main source and sink, respectively (Li et al., 2009; Li et al., 2003;
29 Lupu et al., 2009; Vigouroux et al., 2012; Zeng et al., 2012).

30 With the rapid economic growth in China over the past three decades, the anthropogenic
31 emissions have increased dramatically, raising concerns about worsening air quality in China (Tang
32 et al., 2012; Chan, 2017; Xing et al., 2017; Wang et al., 2017). These emissions are from automobile
33 exhaust, industrial processes and biomass burning. Many researchers have evaluated regional
34 emissions in various pollution regions (e.g., the Jing-Jin-Ji region, the Yangtze River Delta region,
35 and the Pearl River Delta region), but the relative contribution of the biomass burning, automobile
36 exhaust, and industrial processes is seldom mentioned in the literature (Tang et al., 2012; Chan,
37 2017; Wang et al., 2017; Sun et al., 2018a; Xing et al., 2017). This is because both industrial
38 emissions and biomass burning are major sources of the trace gases (e.g. CO, C_2H_6 and CO_2) that
39 were used to evaluate regional emissions in the literature, and it is hard to quantify their relative
40 contribution under the complex pollution condition in China (Chan et al., 2018; Tang et al., 2012;
41 Wang et al., 2017; Xiaoyan et al., 2010; Xing et al., 2017). It has been proved that HCN is an
42 unambiguous tracer of biomass burning emission due to its inactive chemical feature and long
43 lifetime (Rinsland et al., 2002; Zhao et al., 2002). Therefore, measurements of HCN made in
44 polluted troposphere in eastern China at middle latitude are particularly useful in determining the
45 potential biomass burning sources that drive the observed tropospheric HCN seasonality and
46 interannual variability in China.

47 Ground based high-resolution Fourier Transform Spectroscopy (FTIR) measurements of trace
48 gases made by Anhui Institute of Optics and Fine Mechanics, Chinese Academy of Sciences
49 (AIOFM-CAS) at Hefei ($117^\circ 10'\text{E}$, $31^\circ 54'\text{N}$, 30 m a.s.l. (above sea level)) is one of few multiyear
50 time series of trace gases on Asian continent (Sun et al., 2018a; Sun et al., 2018b). These
51 measurements are crucial to understanding global warming, regional pollution, and long term
52 transport. Both HCN and CO are regularly measured at Hefei (32°N) in the FTIR observation
53 routine, influences from biomass burning occurred at a long distance or occurred locally can be
54 assessed.

55 In this study, we analyze the first multiyear measurements of tropospheric HCN in densely
56 populated eastern China. In section 2 the retrieval strategy to derive HCN from high resolution FTIR
57 spectrometry and the methods for a GEOS-Chem tagged CO simulation and potential source



1 contribution function (PSCF) calculation are summarized. In section 3 we present the seasonal and
2 interannual variability of tropospheric HCN columns measured at Hefei (32° N), China and
3 comparisons with NDACC counterparts. The potential sources that drive the observed HCN
4 variability are determined by using the GEOS-Chem tagged CO simulation, the global fire maps
5 and the PSCFs analysis in section 4. The work concludes with a summary in section 5. This study
6 can improve our understanding of regional biomass burning characteristic and transport, and
7 contribute to the evaluation of global nitrogen cycle.

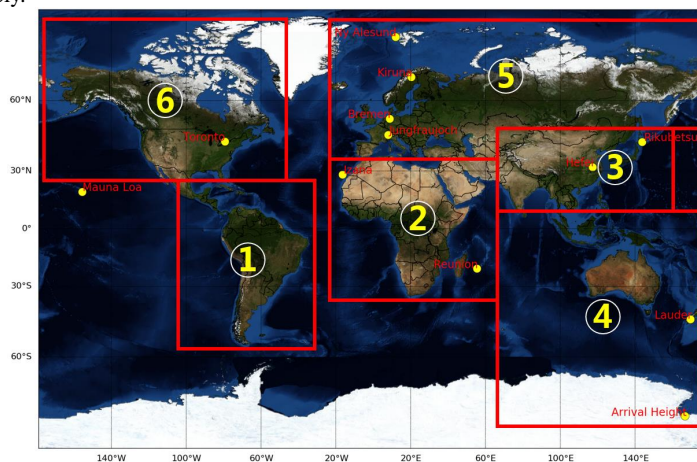
8 2 Methods

9 2 FTIR observations

10 2.1.1 Site description and instrumentation

11 The routine observations of atmospheric trace gases using ground based high-resolution FTIR
12 spectrometer at Hefei (117°10'E, 31°54'N, 30 m a.s.l.) started in July 2014. Location of Hefei site
13 alongside those of the NDACC FTIR stations selected for comparison are shown in Fig.1.
14 Geographical source regions used in the standard GEOS-Chem tagged CO simulation are also
15 marked in Fig.1. Detailed description of Hefei site can be found in Tian et al., 2017. We follow the
16 NDACC (Network for Detection of Atmospheric Composition Change, <http://www.ndacc.org/>, last
17 accessed on 3 June 2019) requirements, and it is planned to apply for acceptance within the NDACC
18 in the future.

19 A Bruker IFS 125 HR with maximum optical path difference (OPD) of 900 cm is used to take
20 the solar spectra (Tian et al., 2017). Defined as 0.9/OPD, this instrument can reach a highest spectral
21 resolution of 0.001 cm⁻¹. However, all mid-infrared (MIR) spectra are recorded with a spectral
22 resolution of 0.005 cm⁻¹ to ensure a higher signal to noise ratio (SNR) and a faster acquisition time.
23 This spectral resolution is sufficient to resolve the optical absorption structure of all gases in the
24 atmosphere. The FTIR spectrometer covered a wide spectral range (about 600 – 4500 cm⁻¹) but,
25 depending on the species, specific detectors and band-pass filters are applied (Sun et al. 2018a). In
26 this study, the instrument is equipped with a KBr beam splitter & InSb detector & filter no.3 centered
27 at 2900 cm⁻¹ for HCN measurements, and a KBr beam splitter & InSb detector & filter no.4 centered
28 at 2400 cm⁻¹ for CO measurements. The entrance field stop size ranged from 0.80 to 1.5 mm to
29 adapt the incident radiation. The number of measurements within a day varies from 1 to 20. In total,
30 there were 651 and 649 days of qualified measurements between 2015 and 2018 for CO and HCN,
31 respectively.



32
33 Fig. 1 Location of Hefei site alongside those of the NDACC FTIR stations (yellow dots) that are selected for
34 comparison. Geographical source regions used in the standard GEOS-Chem tagged CO simulation are also shown.
35 See Table 3 for latitude and longitude definitions

36 2.1.2 Retrieval strategy

37 The SFIT4 (version 0.9.4.4) algorithm is used to retrieve the vertical profiles of CO and HCN
38 (Viatte et al., 2014). Both CO and HCN are standard NDACC species, and we follow the NDACC
39 recommendation for micro windows (MWs) selection and the interfering gases consideration
40 (<http://www.ndaccdemo.org/>, last accessed on 23 May 2019). The retrieval inputs for CO and HCN



1 are summarized in Table 1. Time series of tropospheric CO columns between 2014 and 2017 at
 2 Hefei (32°N) measured from the FTIR have been reported in Sun et al. (2018a) and the detailed
 3 description of CO profile retrieval can be found therein. Time series of tropospheric HCN columns
 4 at Hefei (32°N) are presented for the first time. Temperature and pressure profiles are extracted
 5 from National Centers for Environmental Protection (NCEP) 6-hourly reanalysis data (De Maziere
 6 et al., 2018) and all spectroscopic absorption parameters are prescribed from HITRAN 2008
 7 database (Rothman et al., 2009). The H₂O *a priori* profile is interpolated from the NCEP 6-hourly
 8 reanalysis data and *a priori* profiles of other gases are from the WACCM v6 (Whole-Atmosphere
 9 Community Climate Model) special run for NDACC.

10 Three MWs were used for CO: a strong line at 2057.7–2058 cm⁻¹ and two weak lines at
 11 2069.56–2069.76 cm⁻¹ and 2157.5–2159.15 cm⁻¹ (Sun et al., 2018a). For HCN, two MWs were
 12 used: 3268.00–3268.38 cm⁻¹ and 3287.00–3287.48 cm⁻¹ (Mahieu et al., 1997; Lutsch et al., 2016;
 13 Notholt et al., 2000). In order to minimize the cross absorption interference, profiles of O₃ and N₂O
 14 and columns of H₂O, OCS and CO₂ are simultaneously retrieved in addition to the CO profile.
 15 Profile of H₂O and columns of O₃, C₂H₂, and CH₄ are simultaneously retrieved in addition to the
 16 HCN profile. No de-weighting SNR is used for HCN and a de-weighting SNR of 500 is used in the
 17 three MWs for CO.

18 The diagonal elements of *a priori* profile covariance matrices **S_a** are set to standard deviation
 19 of the WACCM v6 special run for NDACC, and its non-diagonal elements are set to zero. The
 20 diagonal elements of the measurement noise covariance matrices **S_e** are set to the inverse square of
 21 the SNR calculated from each individual spectrum and its non-diagonal elements are set to zero.
 22 The measured instrument line shape (ILS) is included in the retrieval (Hase, 2012; Sun et al., 2018a).

23

Table 1. Retrieval inputs used for CO and HCN.

Gases	CO	HCN
Code	SFIT4 v 0.9.4.4	SFIT4 v 0.9.4.4
Spectroscopic parameters	HITRAN 2008	HITRAN 2008
P, T, H ₂ O profiles	NCEP reanalysis data	NCEP reanalysis data
<i>A priori</i> profiles of all gases except H ₂ O	WACCM v6	WACCM v6
Micro windows for profile retrievals (cm ⁻¹)	2057.7 - 2058 2069.56–2069.76 2157.5–2159.15	3268.00 – 3268.38 3287.00–3287.48
Retrieved interfering gases	O ₃ , N ₂ O, CO ₂ , OCS, H ₂ O	H ₂ O, O ₃ , C ₂ H ₂ , CH ₄
SNR for de-weighting	500	None
S_a	WACCM v6 standard deviation	WACCM v6 standard deviation
S_e	SNR calculated from each individual spectrum within 2526.23 – 2526.62	SNR calculated from each individual spectrum within 3381.16 – 3381.54
ILS	LINEFIT145 analysis	LINEFIT145 analysis
Error analysis	Systematic error: line intensity, line pressure broadening, line temperature broadening, solar zenith angle, background curvature, solar line strength, optical path difference, field of view, phase Random error: -Measurement error -Smoothing error -Interference errors: interfering species, retrieval parameters - Other errors: zero level, temperature	

24 2.1.3 Averaging kernels and error budget

25 The partial column averaging kernels of CO and HCN at selected layers are shown in Fig. 2.
 26 The CO averaging kernels have three maxima at the surface, 7 km, and 14 km, respectively. The
 27 HCN averaging kernels have two maxima at 10 km and 16 km, respectively. Both CO and HCN
 28 retrievals show good vertical sensitivity in the whole troposphere where CO exhibits the best
 29 sensitivity with two maxima in the troposphere (Sun et al., 2018a). We can see in Table 2, the typical
 30 degrees of freedom (DOFS) obtained at Hefei (32°N) over the total atmosphere for CO and HCN
 31 are about 2.8 ± 0.3 (1σ) and 1.3 ± 0.2 (1σ), respectively. In this study, only partial columns of CO
 32 and HCN within a broad layer between surface and 15 km are considered. The selected layer
 33 corresponds roughly to the total troposphere over eastern China, as the mean tropopause height
 34 deduced from NCEP reanalysis data is around 15 km over four seasons. The selected layer
 35 corresponds to 2.3 ± 0.2 (1σ) and 1.0 ± 0.1 (1σ) of DOFS for CO and HCN, respectively.

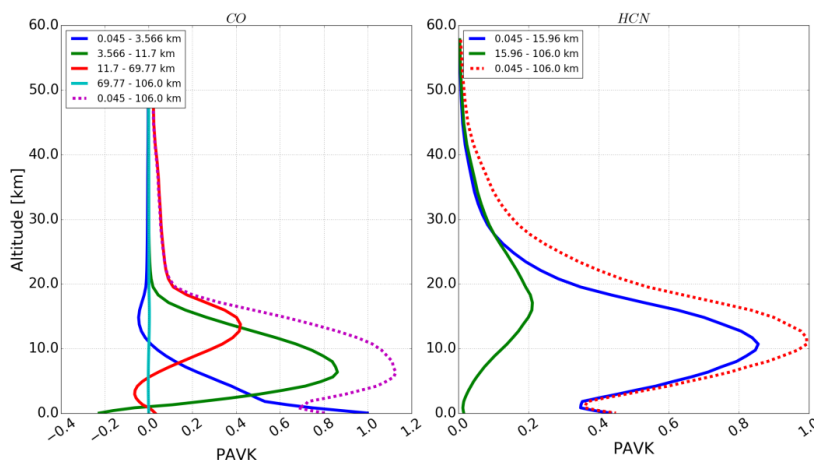


Fig. 2 Partial column averaging kernels (PAVKs) (ppmv / ppmv) for CO and HCN retrievals.

We calculated the error budget following the formalism of (Rodgers, 2000), and separated all error items into systematic error or random error depending on whether they are constant over consecutive measurements, or vary randomly. Table 2 summarizes the random, the systematic, and the combined error budget of tropospheric CO and HCN columns. The error items included in the error budget are listed in Table 1. For CO, the major systematic error is line intensity uncertainty, and the major random error are zero level uncertainty and temperature uncertainty. For HCN, the major systematic error are line intensity uncertainty and line pressure broadening uncertainty, the major random error are smoothing error and measurement error. Total retrieval errors for tropospheric CO and HCN columns between surface and 15 km are estimated to be 8.3 and 14.2%, respectively.

Table 2. Retrieval error budgets and DOFs for tropospheric CO and HCN.

Gases	CO	HCN
Temperature uncertainty	2.5%	0.2%
Zero level uncertainty	5.2%	1.5%
Retrieval parameters uncertainty	< 0.1%	2.0%
Interfering species uncertainty	< 0.1%	1.3%
Measurement Error	< 0.1%	6.8%
Smooth Error	0.1%	11.0%
Total Random Error	5.7%	13.2%
Background curvature uncertainty	< 0.1%	*
Optical path difference uncertainty	< 0.1%	< 0.1%
Field of view uncertainty	< 0.1%	< 0.1%
Solar line strength uncertainty	< 0.1%	< 0.1%
Phase uncertainty	*	< 0.1%
Solar zenith angle uncertainty	0.1%	< 0.1%
Line temperature broadening uncertainty	0.13%	0.3%
Line pressure broadening uncertainty	0.87%	3.5%
Line intensity uncertainty	6.0%	3.7%
Total Systematic Error	6.1%	5.1%
Total Errors	8.3%	14.2%
DOFS (-)	2.2	1.0

* Not included into error budget since they are retrieved together with the target gas

2.2 GEOS-Chem tagged simulation

To interpret the influence of biomass burning sources on HCN columns at Hefei (32°N), the GEOS-Chem chemical transport model is used (<http://geos-chem.org/>; Bey et al., 2001b) in a tagged simulation of CO at a horizontal resolution of 2°×2.5° with 47 vertical hybrid levels. GEOS-Chem version 12.2.1 was used and driven by the GEOS-FP assimilated meteorological data observations from the Goddard Earth Observing System (GEOS) of the NASA Global Modeling and Assimilation Office. For driving the GEOS-Chem model, the GEOS-FP meteorological data with a native horizontal resolution of 0.25° latitude × 0.3125° longitude were downgraded to 2° latitude × 2.5° longitude and a vertical resolution of 72 hybrid levels (extending from surface to 0.01 hPa). The



1 temporal resolution of surface variables and boundary layer height are 1hr and other variables are
2 3hr.

3 The GEOS-Chem simulation was initialized with a 1-year spin-up from July 2014 to July 2015.
4 Chemical and transport operator time-steps of 1 hr and 10 min, respectively, were used. Biomass
5 burning emissions are from GFASv1.2 (Global Fire Assimilation System, Kaiser et al., 2012;
6 Giuseppe et al., 2018) which assimilates Moderate Resolution Imaging Spectroradiometer (MODIS)
7 burned area and fire radiative power (FRP) products to estimate emissions for open fires. GFASv1.2
8 emissions have a $0.1^\circ \times 0.1^\circ$ horizontal resolution with 3-hourly temporal resolution. GFAS was
9 chosen for the availability of emissions over the analysis period from 2015 - 2018. Global
10 anthropogenic and biofuel emissions are from the Community Emissions Data System (CEDS)
11 inventory (Hoesly et al., 2018). In particular, the latest MEIC (the Multi-resolution Emission
12 Inventory for China) inventory is used to provide Chinese anthropogenic emissions (Li et al., 2017).
13 Biogenic emissions of precursor VOCs are from the Model of Emissions of Gases and Aerosols
14 from Nature (MEGANv2.1; Guenther et al., 2012) and biofuel emissions are taken from Yevich
15 and Logan (2003). The main loss mechanism for CO is from photochemical oxidation by the hydroxyl
16 radical (OH). The OH fields are prescribed in the tagged CO simulation and were obtained from the
17 TransCom experiment (Patra et al., 2011) which implements semi-empirically calculated
18 tropospheric OH concentrations from Spivakovsky et al. (2000) to reduce the high bias of OH from
19 the GEOS-Chem full-chemistry simulation (Shindell et al., 2006). Surface emissions in GEOS-
20 Chem are released within the boundary layer, and boundary layer mixing is implemented using the
21 non-local mixing scheme of Holtslag and Boville (1993). Biomass emissions are released by
22 uniformly distributing emissions from the surface to the mean altitude of maximum injection based
23 on the injection height information as described in Rémy et al. (2017) which includes an injection
24 height parameterization by Sofiev et al. (2012) and a plume rise model by Freitas et al. (2007).

25 GEOS-Chem version 12.2.1 tagged CO simulation includes the improved secondary CO
26 production scheme of Fisher et al. (2017), which assumes production rates of CO from CH₄ and
27 NMVOC (non-methane volatile organic compounds) oxidation from a GEOS-Chem full-chemistry
28 simulation therefore reducing the mismatch between the CO-only simulation and the full-chemistry
29 simulation.

30 The tracers of anthropogenic, biomass burning, CH₄ and NMVOC oxidations are implemented
31 following the standard GEOS-Chem tagged CO simulation (Giglio et al., 2013). In this study, we
32 don't investigate the influence of each individual anthropogenic and oxidation source tracer. For
33 investigation of the influence of biomass burning sources, the regional definitions of all biomass
34 burning tracers are shown in Fig. 1 and tabulated in Table 3.

35 Table 3. Regional definitions of all biomass burning tracers implemented in the standard GEOS-Chem tagged CO
36 simulation

No.	Tracer	Description	Region
1	SA	Biomass burning CO emitted over South America	112.5°W - 32.5°W; 56°S - 24°N
2	AF	Biomass burning CO emitted over Africa	17.5°W - 70.0°E; 48.0°S - 36.0°N
3	SEAS	Biomass burning CO emitted over Southeast Asia	70.0°E - 152.5°E; 8.0°N - 45.0°N
4	OCE	Biomass burning CO emitted over Oceania	70.0°E - 170.0°E; 90.0°S - 8.0°N
5	EUBA	Biomass burning CO emitted over Europe and Boreal Asia	17.5°W - 72.5°E; 36.0°N - 45.0°N and 17.5°W - 172.5°E; 45.0°N - 88.0°N
6	NA	Biomass burning CO emitted over North America	173°W - 50°W; 24.0°N - 88.0°N

37 2.3 Potential source contribution function

38 The potential source contribution function (PSCF) assumes that back trajectories arriving at
39 times of higher concentrations likely point to the more significant pollution directions (Ashbaugh
40 et al., 1985). PSCF has been applied in many studies to locate air masses associated with high levels
41 of air pollutants (Kaiser et al., 2007; Dimitriou and Kassomenos, 2015; Yin et al., 2017). In this
42 study, PSCF values were calculated using back trajectories that were calculated by HYSPLIT. The
43 top of the model was set to 10 km. The PSCF values for the grid cells in the study domain were
44 based on a count of the trajectory segment that terminated within each cell (Ashbaugh et al., 1985).



1 The number of endpoints that fall in the i_j^{th} cell is designated n_{ij} . The number of endpoints for the
 2 same cell having arrival times at the sampling site corresponding to concentrations higher than an
 3 arbitrarily set criterion is defined to be m_{ij} . In this study, we calculated the PSCF values based on
 4 trajectories corresponding to concentrations that exceeded the monthly mean level of tropospheric
 5 HCN column during measurement. The PSCF value for the i_j^{th} cell is then defined as:

$$PSCF_{ij} = m_{ij}/n_{ij} \quad (1)$$

7 The PSCF value can be interpreted as the conditional probability that the concentrations of a
 8 given analyte greater than the criterion level are related to the passage of air parcels through the i_j^{th}
 9 cell during transport to the receptor site. That is, cells with high PSCF values are associated with
 10 the arrival of air parcels at the receptor site that have concentrations of the analyte higher than the
 11 criterion value. These cells are indicative of areas of ‘high potential’ contributions for the constituent.

12 Identical $PSCF_{ij}$ values can be obtained from cells with very different counts of back-trajectory
 13 points (e.g., grid cell A with $m_{ij} = 400$ and $n_{ij} = 800$ and grid cell B with $m_{ij} = 4$ and $n_{ij} = 8$). In this
 14 extreme situation grid cell A has 100 times more air parcels passing through than grid cell B.
 15 Because of the sparse particle count in grid cell B, the PSCF values are more uncertain. To account
 16 for the uncertainty due to low values of n_{ij} , the PSCF values were scaled by a weighting function
 17 W_{ij} (Polissar et al., 1999). The weighting function reduced the PSCF values when the total number
 18 of endpoints in a cell was less than approximately 3 times the average value of the end points per
 19 cell. In this case, W_{ij} was set as follows:

$$W_{ij} = \begin{cases} 1.00 & n_{ij} > 3N_{ave} \\ 0.70 & 3N_{ave} > n_{ij} > 1.5N_{ave} \\ 0.42 & 1.5N_{ave} > n_{ij} > N_{ave} \\ 0.05 & N_{ave} > n_{ij} \end{cases} \quad (2)$$

21 where N_{ave} represents the mean n_{ij} of all grid cells. The weighted PSCF values were
 22 obtained by multiplying the original PSCF values by the weighting factor.

23 3 FTIR time series and comparisons with NDACC counterparts

24 The new HCN data are compared with the counterparts regularly measured at eleven NDACC
 25 stations to investigate the representativeness of the observation site at Hefei (32°N) in polluted
 26 eastern China. These NDACC stations cover over a wide latitude range from 77.8°S to 78.9°N and
 27 a wide longitude range from 79°W to 170°E (<http://www.ndaccdemo.org/>, last access on 19 July
 28 2019). Most of these NDACC stations use the same instrument and retrieval algorithm as those of
 29 Hefei (32°N). Alternatively, the high resolution spectrometers Bruker 125M, 120HR, or Bomem
 30 DA8 and the retrieval algorithm PROFFIT are used in other stations. It has been demonstrated that
 31 the profiles derived from these different instruments and algorithms are in excellent agreement
 32 (Hase et al., 2004; De Maziere et al., 2018). In addition, we show the time series of tropospheric
 33 CO columns, also measured with FTIR spectrometer, because we will discuss the correlation
 34 between HCN and CO, and quantify the influence of biomass burning sources on HCN columns at
 35 Hefei (32°N) by using a tagged CO simulation. The upper limit of 15 km is above the tropopause at
 36 most of the NDACC stations. For most NDACC stations, the surface – 15 km layer is a mixture of
 37 the total troposphere and a part of stratosphere. However, we did not find major changes in the
 38 results of this study when choosing a lower upper limit such as 12 km. Thus we have chosen the
 39 same upper limits for all stations. The geolocations of all FTIR stations and their seasonal maximum,
 40 minimum and variabilities are summarized in Table 4.

41 Table 4. Tropospheric HCN and CO columns at Hefei (32°N), China from 2015 to 2018 alongside those of the
 42 NDACC FTIR stations. All stations are organised as a function of decreasing latitude.

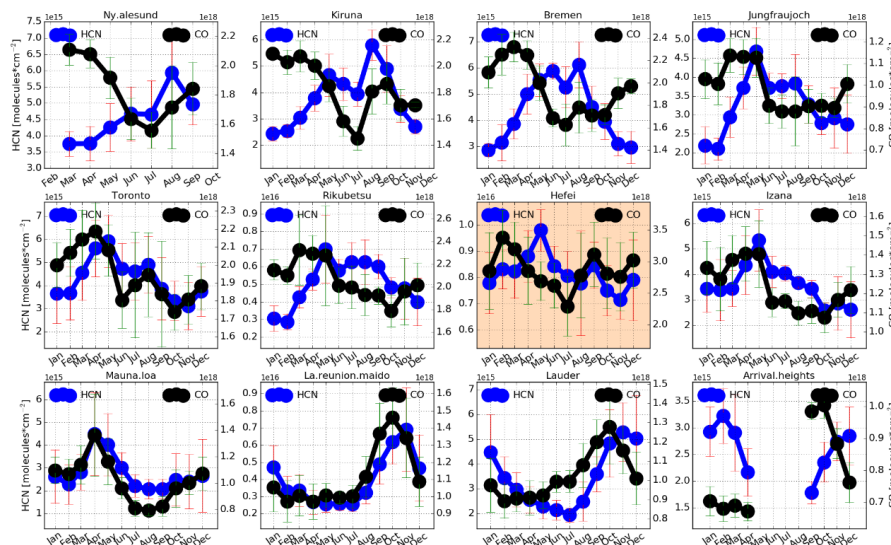
Station	Location (Lon., Lat., Alt. in km)	Instrument	Algorithm	Maximum (molecules cm ⁻²)		Minimum (molecules cm ⁻²)	
				HCN (10 ¹⁵)	CO (10 ¹⁸)	HCN (10 ¹⁵)	CO (10 ¹⁸)
Ny Alesund	(12°E, 79°N, 0.02)	125HR	SFIT4	5.94 ± 1.20 (August)	2.11 ± 0.11 (March)	3.75 ± 0.37 (March)	1.56 ± 0.12 (July)
Kiruna	(20°E, 68°N, 0.42)	125HR	PROFFIT	5.81 ± 0.58 (August)	2.1 ± 0.01 (January)	2.43 ± 0.27 (January)	1.45 ± 0.09 (July)
Bremen	(9°E, 53°N, 0.03)	125HR	SFIT4	6.11 ± 0.87 (August)	2.32 ± 0.13 (March)	2.85 ± 0.25 (January)	1.63 ± 0.19 (July)
Jungfraujoch	(8°E, 46.5°N, 3.58)	125HR	SFIT4	4.68 ± 0.63 (May)	1.14 ± 0.08 (March)	2.1 ± 0.29 (February)	0.88 ± 0.08 (July)
Toronto	(79°W, 44°N, 0.17)	Bomem DA8	SFIT4	5.92 ± 1.13 (May)	2.19 ± 0.15 (April)	3.12 ± 1.02 (November)	1.74 ± 0.1 (October)



Rikubetsu	(144°E, 43°N, 0.38)	125HR	SFIT4	7.0 ± 1.92 (May)	2.32 ± 0.31 (March)	2.86 ± 0.44 (February)	1.79 ± 0.14 (October)
Hefei	(117°E, 32°N, 0.03)	125HR	SFIT4	9.8 ± 0.78 (May)	3.38 ± 0.43 (February)	7.16 ± 0.75 (November)	2.29 ± 0.48 (July)
Izana	(16°W, 28°N, 2.37)	125HR	PROFFIT	5.33 ± 1.2 (May)	1.41 ± 0.14 (April)	2.59 ± 0.28 (October)	1.1 ± 0.08 (October)
Mauna Loa	(24°W, 20°N, 3.40)	125M	SFIT4	4.49 ± 1.8 (April)	1.36 ± 0.31 (April)	2.07 ± 0.43 (August)	0.8 ± 0.04 (August)
La Reunion Maido	(55°E, 21°S, 2.16)	125HR	SFIT4	6.91 ± 2.45 (November)	1.46 ± 0.17 (October)	2.56 ± 0.48 (May)	1.0 ± 0.1 (April)
Lauder	(170°E, 45°S, 0.37)	120HR	SFIT4	5.29 ± 1.18 (November)	1.28 ± 0.19 (October)	1.94 ± 0.28 (July)	0.89 ± 0.09 (February)
Arrival Heights	(167°E, 78°S, 0.2)	120HR	SFIT4	3.22 ± 0.51 (February)	1.0 ± 0.04 (October)	1.78 ± 0.21 (September)	0.67 ± 0.03 (April)

11 3.1 Seasonal variation

12 The monthly means of the tropospheric CO and HCN columns at the twelve FTIR stations are
 13 shown in Fig. 3. As commonly observed at Hefei (32°N), three monthly mean peaks are evident for
 14 tropospheric HCN and CO columns. The magnitude of the tropospheric HCN peak at Hefei (32°N)
 15 in May > September > December. While for tropospheric CO column, the magnitude of the peak at
 16 Hefei (32°N) in February > September > December. For tropospheric HCN and CO columns, the
 17 timing of the monthly mean maximum and minimum are different, but the timing of the smaller two
 18 monthly mean peaks are the same. The tropospheric CO and HCN columns at Hefei (32°N) show
 19 similar seasonal variability throughout the year except March to May, when the variability is
 20 opposite. The biggest contrast in terms of seasonal cycle occurs in May.



11 Fig. 3. Monthly means of the tropospheric CO and HCN columns at Ny Alesund, Kiruna, Bremen, Jungfraujoch,
 12 Toronto, Rikubetsu, Hefei, Izana, Mauna Loa, La Reunion Maido, Lauder, and Arrival Heights from 2015 to 2018.
 13 Vertical error bars represent 1σ within that month. All stations are organised as a function of decreasing latitude.

14 The tropospheric HCN and CO columns at Hefei (32°N) are higher than the NDACC FTIR
 15 observations (see Fig. A1). The tropospheric HCN column reached a maximum of $(9.8 \pm 0.78) \times$
 16 10^{15} molecules/cm² in May and a minimum of $(7.16 \pm 0.75) \times 10^{15}$ molecules/cm² in November.
 17 The tropospheric CO column reached a maximum of $(3.38 \pm 0.43) \times 10^{18}$ molecules/cm² in February
 18 and a minimum of $(2.29 \pm 0.48) \times 10^{18}$ molecules/cm² in July (Table 4). In comparison, the seasonal
 19 maxima and minima of tropospheric HCN columns at the selected NDACC FTIR stations varied
 20 over (3.22 ± 0.51) to $(7.0 \pm 1.92) \times 10^{15}$ molecules/cm² and (1.78 ± 0.21) to $(3.75 \pm 0.37) \times 10^{15}$
 21 molecules/cm², respectively. The seasonal maxima and minima of tropospheric CO columns at the
 22 selected NDACC FTIR stations varied over (1.0 ± 0.04) to $(2.32 \pm 0.31) \times 10^{18}$ molecules/cm² and
 23 (0.67 ± 0.03) to $(1.79 \pm 0.14) \times 10^{18}$ molecules/cm², respectively (Table 4).

24 In the northern hemisphere, the timing of the seasonal maxima for tropospheric HCN columns

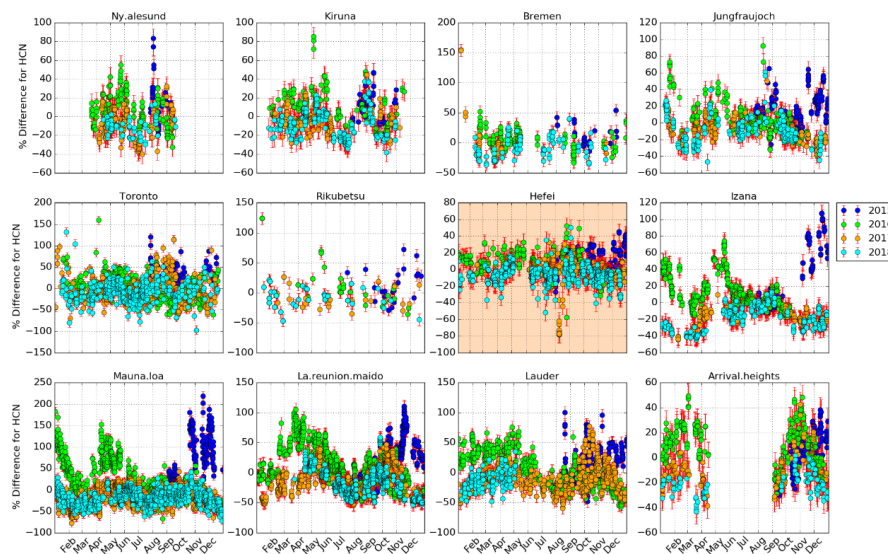


1 generally occur in spring or summer, and for CO occur in winter or spring. While in the southern
2 hemisphere, the timing of the seasonal maxima for both tropospheric HCN and CO columns occur
3 in autumn or winter.

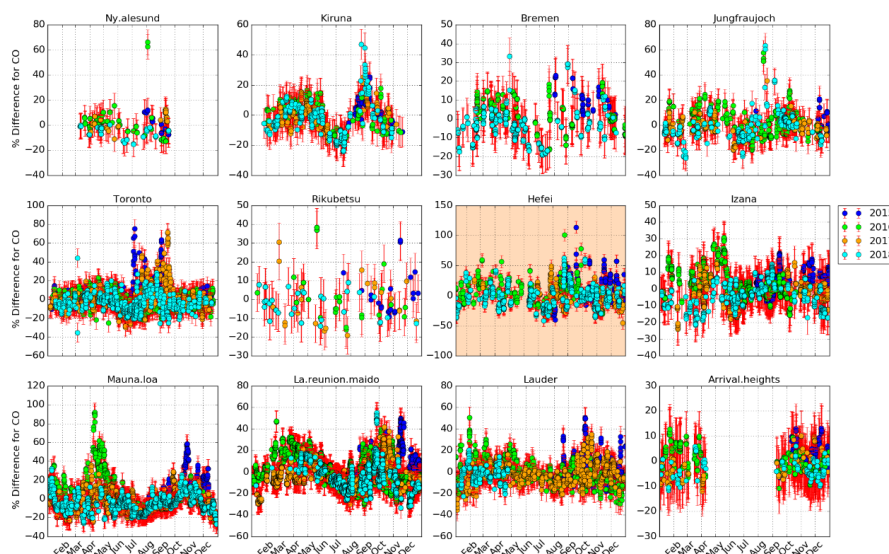
4 3.2 Interannual variability and enhancement

5 In order to study the interannual variability of HCN and CO, fractional differences in the
6 tropospheric HCN and CO columns relative to their seasonal mean values represented by the cosine
7 fitting at the twelve FTIR stations are shown in Fig.4 and Fig.5, respectively. Enhancements of both
8 tropospheric HCN and CO columns between September 2015 and July 2016 at Hefei (32°N) were
9 observed compared to the measurements in other years. For HCN, the magnitude of the
10 enhancement ranges from 5 to 46% with an average of 26%. The significant enhancements occurred
11 in December 2015 and May 2016 with peaks of 46% and 38%, respectively. By contrast, the
12 magnitude of the enhancement in tropospheric CO column at Hefei (32°N) between September 2015
13 and July 2016 ranges from 4 to 59% with an average of 27%.The tropospheric CO columns were
14 elevated over its seasonal means by more than 20% from March to April 2016. In addition, an
15 enhancement magnitude of more than 40% were occasionally observed in August and September
16 for both HCN and CO at Hefei (32°N).

17 The enhancements of both tropospheric HCN and CO columns within the same period were
18 also observed at the selected NDACC stations except Ny Alesund (79°N) and Kiruna (68°N). The
19 winter enhancements were not shown over Ny Alesund (79°N) and Kiruna (68°N) because of the
20 polar night in the Arctic which interrupted the observations in winter. The magnitude of the
21 enhancement in tropospheric HCN column at the selected NDACC stations between September
22 2015 and July 2016 ranges from 3 to 213%, and for CO ranges from 4 to 62%.



23
24 Fig.4. Fractional difference in the partial columns (surface - 15 km) of HCN from 2015 to 2018 at Ny Alesund,
25 Kiruna, Bremen, Jungfraujoch, Toronto, Rikubetsu, Hefei, Izana, Mauna Loa, La Reunion Maito, Lauder, and
26 Arrival Heights relative to their seasonal mean values. Vertical error bars represent the estimated retrieval errors.
27 All stations are organised as a function of decreasing latitude.



1
2 Fig.5. The same as Fig.4 but for CO.

3 3.3 Correlation with CO and enhancement ratios

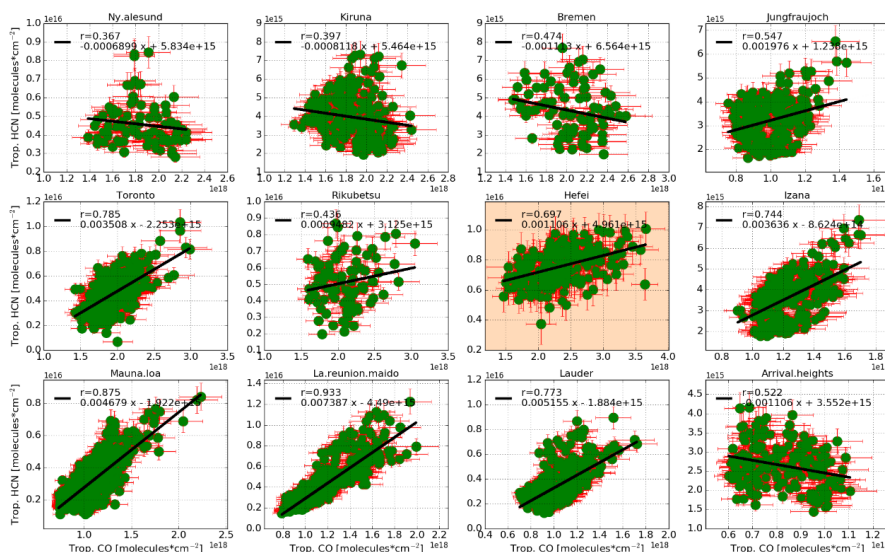
4 The tropospheric HCN columns at the twelve FTIR stations have been plotted against the
5 coincident CO partial columns (Fig.6). In Fig.7, the correlations between the tropospheric HCN and
6 CO columns at Hefei (32°N) for all spectra recorded throughout the year (gray dots) and those
7 recorded within the selected periods (green dots) are compared. We followed the least squares
8 procedure of York et al., 2004 to proceed a linear regression for the coincident measurements, and
9 incorporated the errors in both ordinal and abscissa coordinates into the uncertainty estimation.

10 Since different atmospheric chemistry processes control the abundance of CO and HCN,
11 moderate overall correlations between HCN and CO tropospheric columns were present at
12 Jungfraujoch (47°N) and Rikubetsu (43°N), and negative overall correlations were present at Ny
13 Alesund (79°N), Kiruna (68°N), Bremen (53°N), and Arrival Heights (78°S). However, high
14 correlation of these two species were seen at Toronto (44°N), Hefei (32°N), Izana (28°N), Mauna
15 Loa (20°N), La Reunion Maido (21°S), and Lauder (45°S) throughout the year probably because
16 the portion of the fire-affected seasonal measurements at these stations are larger than those at other
17 stations (Fig.6). For the measurements at Hefei (32°N), the high correlations between HCN and CO
18 tropospheric columns deduced from the measurements without March and April ($R=0.67$, Fig.7 (a)),
19 in May ($R=0.69$, Fig.7 (b)), in September ($R=0.77$, Fig.7 (c)), and in December ($R=0.65$, Fig.7 (d))
20 are consistent with that deduced from all measurements ($R=0.70$) (Table 5). However, the
21 correlation slope for the May, September, and December tropospheric columns differ from the
22 annual one, indicating different biomass burning sources in different periods.

23 For fire-affected measurements, the slope $\Delta\text{HCN}/\Delta\text{CO}$ defined as enhancement ratio (EnhR_{HCN})
24 is an important parameter in quantification of biomass burning emissions (Holzinger et al., 1999;
25 Lutsch et al., 2016; Rinsland et al., 2002; Viatte et al., 2015; Vigouroux et al., 2012; Zhao et al.,
26 2000). Depending on the burnt biomaterials, fire type, the phase of the fire, and the travel time of
27 the plumes, the reported EnhR_{HCN} varied by 2 orders of magnitude. The mean EnhR_{HCN} of 1.34×10^{-3}
28 at Hefei (32°N) falls between the wide range of the HCN/CO ratios measured in laboratory ($0.4 -$
29 7.1×10^{-3} in the work of (Yokelson et al., 1997) and $0.4 - 2.6 \times 10^{-3}$ in the work of (Holzinger et al.,
30 1999), and $0.94 - 7.4 \times 10^{-3}$ in the NDACC FTIR measurement counterparts (Fig. 6). The mean
31 EnhR_{HCN} at Hefei (32°N) is close to that at Rikubetsu (43°N) indicates these two Asian stations
32 share similar biomass burning sources through the year. The mean EnhR_{HCN} at Hefei (32°N) is lower
33 than those measured at Jungfraujoch (47°N), Toronto (44°N), Izana (28°N), Mauna Loa (20°N),
34 Lauder (45°S), and La Reunion Maido (21°S) because the emissions of crop residue burning which
35 dominates the HCN enhancements at Hefei (32°N) is lower than those of the boreal or tropical forest
36 burning, which account for the HCN enhancements at aforementioned NDACC stations (Akagi et al., 2011;
37 Akagi et al., 2012; Rinsland et al., 2007; Vigouroux et al., 2012). On the other hand, the



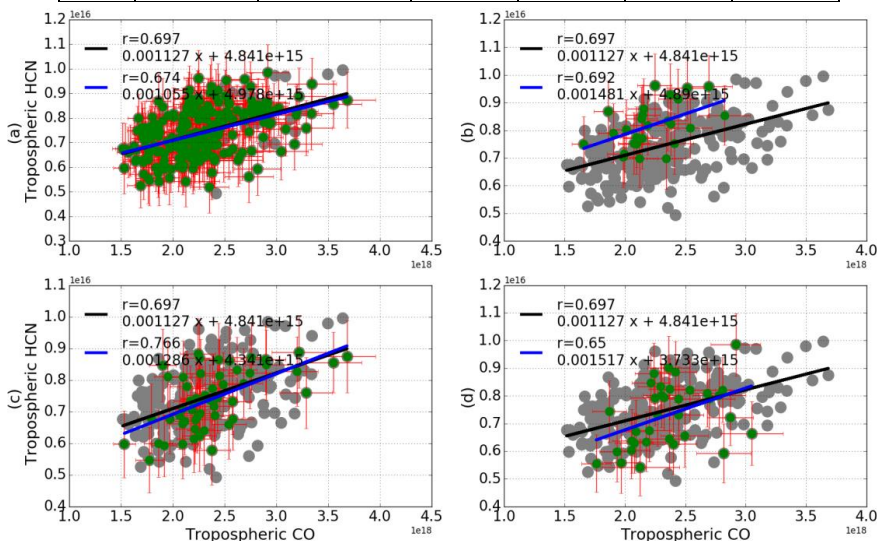
1 Hefei (32°N) site located in the densely populated part of China, emissions of fossil fuel combustion
 2 such as automobile exhaust and industrial processes could elevate the CO background level and
 3 hence lessen the EnhR_{HCN} .



4
 5 Fig. 6. Correlation plots of daily mean partial columns (surface - 15 km) of HCN versus CO (molecules/cm²). The
 6 linear equation of the fit and the resulting correlation coefficient r are shown. The black line is a linear least-squares
 7 fit of respective data. All stations are organised as a function of decreasing latitude. Error bars represent the retrieval
 8 uncertainties.

9 Table 5. Correlation between HCN and CO tropospheric columns within each selected period at Hefei (32°N),
 10 China. N is the number of points, R is the correlation coefficient and EnhR_{HCN} is the enhancement ratio.

Gas	Period	without March and April	May	September	December	Mean
HCN	N	239	26	56	35	-
	R	0.67	0.69	0.77	0.65	0.7
	$\text{EnhR} \times 10^{-3}$	1.06	1.48	1.29	1.52	1.34



11
 12 Fig. 7. Correlation plots of daily mean tropospheric columns of HCN versus CO (molecules/cm²) at Hefei (32°N).



1 The gray dots represent all measurements and the green dots represent the measurements within the selected period:
2 (a) measurements without March and April; (b) measurements in May; (c) measurements in September; (d)
3 measurements in December. The linear equation of the fit and the resulting correlation coefficient r are shown. The
4 black line is a linear least-squares fit of the gray data and the blue line is for the green data. Error bars represent the
5 retrieval uncertainties.

6 **4 Source attribution**

7 In order to determine what drives the seasonality and interannual variability of tropospheric
8 HCN in eastern China, it is necessary to match the observed time series with actual biomass burning
9 events, and show that the generated plumes are capable of travelling to the observation site. We did
10 this by using various independent data sets.

11 1. The 1-hourly instantaneous CO VMR (volume mixing ratio) profiles of the tracers listed in
12 Table 3 provided by a GEOS-Chem tagged CO simulation performed as described in Section 2.2.

13 2. The global fire atlas data archived by the Fire Information for Resource Management System
14 (FIRMS) which generates fire information from NASA's Moderate Resolution Imaging
15 Spectroradiometer (MODIS) and NASA's Visible Infrared Imaging Radiometer Suite (VIIRS)
16 (<https://firms.modaps.eosdis.nasa.gov/download/>, last access on 23 May 2019). We have only taken
17 the fire number with a retrieval confidence value of larger than 60% into account.

18 3. Three dimensional kinematic back trajectories at designated elevations calculated by the Air
19 Resources Laboratory (ARL, <http://ready.arl.noaa.gov/HYSPLIT.php>, last accessed on 23 May
20 2019) Hybrid Single Particle Lagrangian Integrated Trajectory (HYSPLIT) model using Global
21 Data Assimilation System (GDAS) meteorological fields (<https://ready.arl.noaa.gov/gdas1.php>, last
22 accessed on 23 May 2019).

23 4. The PSCF values calculated by MeteoInfo as described in Section 2.3 using HYSPLIT back
24 trajectories (<http://meteothink.org/index.html>, last accessed on 17 December 2019).

25 **4.1 Attribution for the seasonality**

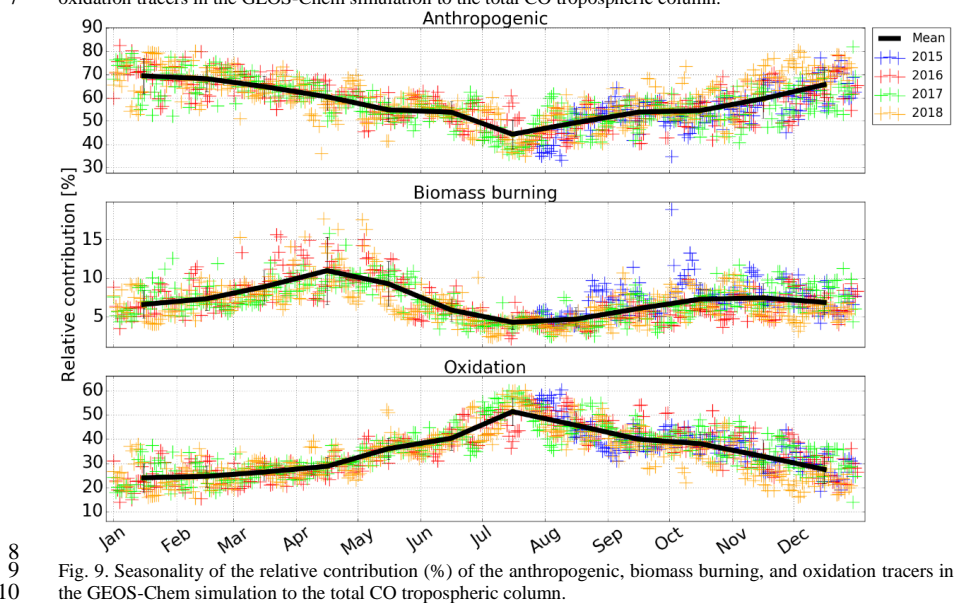
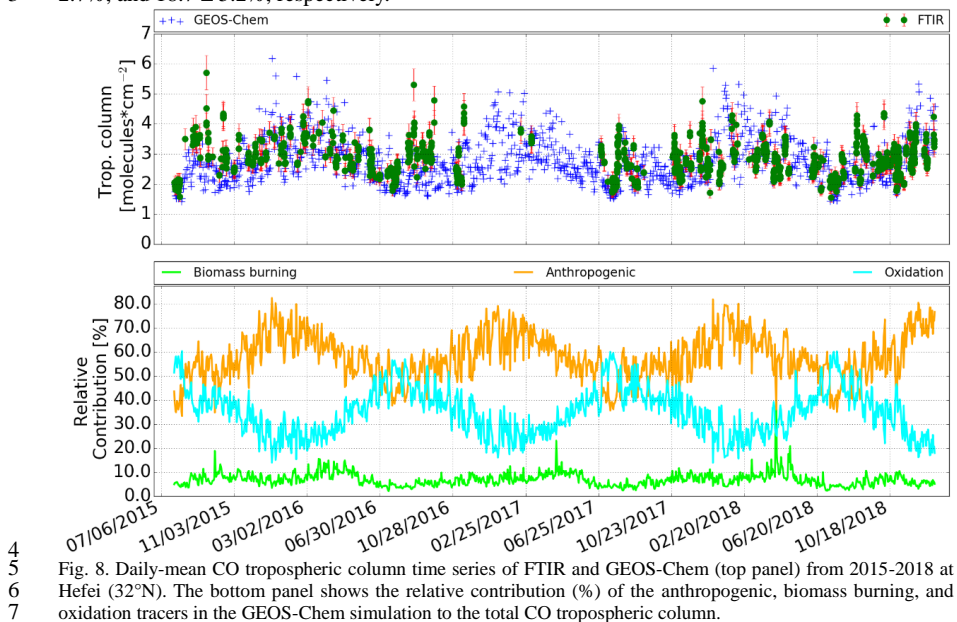
26 The GEOS-Chem tagged CO simulation provides a means of evaluating the contribution of
27 CO from anthropogenic, biomass burning and oxidation sources to the measured CO columns at
28 Hefei (32°N). Source attribution is performed as follows. First, the GEOS-Chem CO VMR profiles
29 of all tracers in the grid box containing the Hefei (32°N) site were converted to partial column
30 profiles and linearly interpolated and regrided onto the FTIR vertical retrieval grid. This was
31 necessary in order to account for the differences in the vertical levels of the model and the FTIR
32 (Barret et al., 2003). Then, The GEOS-Chem CO partial column profiles are smoothed by the
33 normalized FTIR CO total column averaging kernel following Rodgers and Connor (2003). The
34 GEOS-Chem CO profiles, FTIR CO profiles and total column averaging kernels are daily averaged
35 and the daily averaged GEOS-Chem profiles are subsequently smoothed. Fig.8 shows the daily-
36 averaged GEOS-Chem and FTIR CO tropospheric columns (surface-15 km) for the simulation
37 period from 2015 - 2018. The relative contribution of anthropogenic, biomass burning and oxidation
38 tracers are also shown. The GEOS-Chem and FTIR CO tropospheric columns are in good agreement.

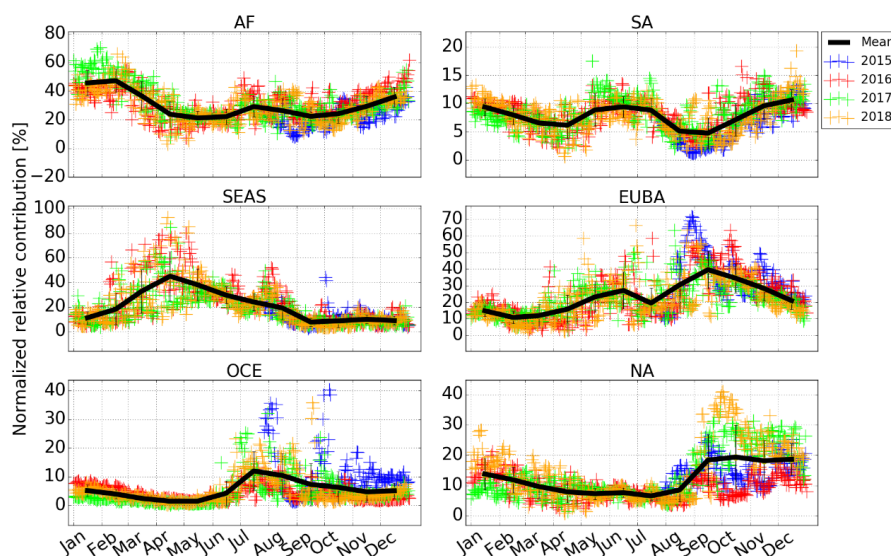
39 The combination of the anthropogenic source and the oxidations of CH₄ and NMVOCs is the
40 greatest contribution to the tropospheric CO column at Hefei (32°N). The magnitude of this
41 combination source varies over 80 to 95% throughout the year. In contrast, the magnitude of biomass
42 burning source varies over 5 to 20%. As shown in Fig.9, the anthropogenic, biomass burning and
43 oxidation sources are all seasonal dependent due to the magnitude of the emissions and the influence
44 of seasonally variable transport. The onset of the anthropogenic contribution begins in July with a
45 maximum in December. In contrast to the anthropogenic influence, the onset of the oxidation
46 contribution begins in January with a maximum in July, as a result of maximum NMVOC emissions
47 in Summer (Sun et al., 2018b). For biomass burning contribution, two onsets were observed. One
48 begins in January with a maximum in April and the other one begins in July with a maximum in
49 October.

50 After normalizing each biomass burning tracer listed in Table 3 to the total biomass burning
51 contribution, the normalized relative contribution of each individual biomass burning tracer to the
52 total biomass burning associated CO tropospheric column was obtained in Fig.10. The results show
53 that the seasonal maxima in May is largely due to the influence of SEAS biomass burning ($41 \pm$
54 13.1%). Moderate contributions from EUBA ($21 \pm 9.3\%$) and AF ($22 \pm 4.7\%$), and small
55 contributions from SA ($7.8 \pm 2.9\%$), OCE ($1.5 \pm 0.8\%$), and NA ($7.7 \pm 1.9\%$) are also observed. The
56 seasonal maxima in September is largely due to the influence of EUBA ($38 \pm 11.3\%$) and AF ($26 \pm$
57 6.7%) biomass burnings. Remaining contributions are from SA ($5.1 \pm 2.7\%$), SEAS ($14 \pm 3.3\%$),



1 OCE ($8.9 \pm 7.4\%$), and NA ($13.8 \pm 8.4\%$). For the seasonal maxima in December, contributions
2 from AF, SA, SEAS, EUBA, OCE, and NA are $36 \pm 7.1\%$, $11 \pm 1.9\%$, $11 \pm 3.6\%$, $21 \pm 5.2\%$, $4.8 \pm$
3 2.7% , and $18.7 \pm 5.2\%$, respectively.





1
2 Fig. 10. Seasonality of the normalized relative contribution (%) of the AF, SA, SEAS, EUBA, OCE, and NA biomass
3 burning tracers in the GEOS-Chem simulation to the total biomass burning associated CO tropospheric column.

4 4.2 Attribution for transport pathway

5 For each seasonal enhancement of the tropospheric HCN, transport pathway is determined as
6 follows. First, the GEOS-Chem tagged CO simulation is used to calculate the relative contribution
7 of each biomass burning tracer (Fig. 10). For the tracer with a high contribution, the FIRMS global
8 fire map is used to search for potential fire events occurred before the timing of tropospheric HCN
9 enhancement within one month period. Then, we generated an ensemble of HYSPLIT back
10 trajectories with different travel times and arrival altitudes to judge whether these plumes are
11 capable of travelling to the observation site. For example, for each intensive biomass burning event
12 detected at a specific period, we generated ten back trajectories at different arrival altitudes ranging
13 from 1.5 to 12 km, and modified the end time of these back-trajectories within one day of the
14 observed enhancement. If the back-trajectories intersect a region where the FIRMS fire data
15 indicates an intensive fire event and the travel duration is within a reasonable range, then this
16 specific fire event could contribute to the observed enhancements at Hefei (32°N) in eastern China.
17 The transport pathway for this enhancement is finally determined.

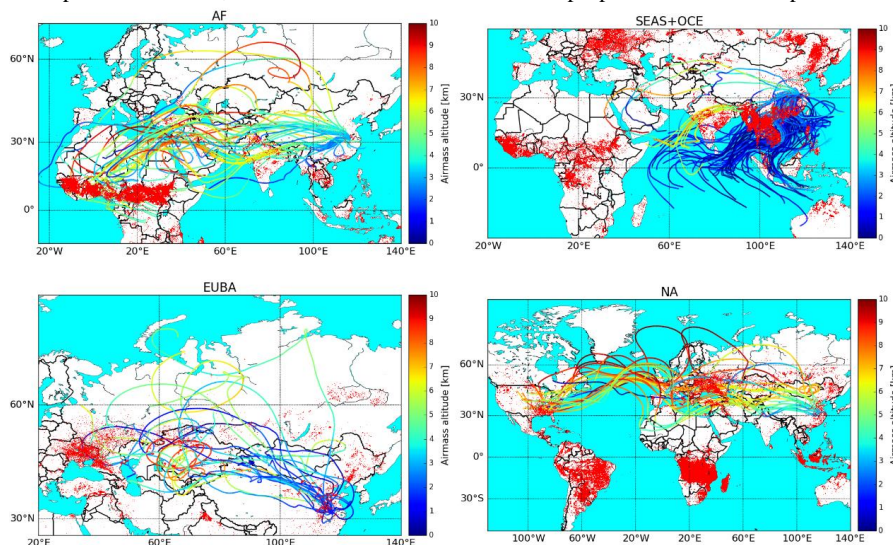
18 Fig. 11 demonstrates travel trajectories of the plumes occurred in AF, SEAS & OCE, EUBA,
19 and NA that reached Hefei (32°N) through long range transport. Fig. 12 shows the PSCFs calculated
20 using 13-day HYSPLIT back trajectories that are coincident with the FTIR measurement time. The
21 eastern China, South Asia, Central Asia, Eastern Europe, and Northern Africa had high PSCF
22 weight values in both the first and second half year. The large areas of Southeastern Asian countries
23 including Philippines, Malaysia, and Indonesia, and the Eastern North America were the additional
24 regions with potentially high PSCF weight values in the second half year. Generally, trajectories
25 with the same travel time in the second half year are longer than those in the first half year, resulting
26 in broader areas with potentially high PSCF weight values.

27 As Figs. 13 and 14 shown, the seasonal biomass burning typically occurs in July – September
28 in southern Africa and in November – February in central Africa. These AF emissions can be
29 transported to eastern China along with the southwestern wind which contributed 25 – 45% of the
30 tropospheric HCN in these periods. The seasonal biomass burning typically occurs in March – May
31 and July – November in central Europe, and in June – September in Siberia. These EUBA emissions
32 can be transported to eastern China along with the northwestern or northern wind which contributed
33 27 – 40% of the tropospheric HCN in these periods. The seasonal biomass burning typically occurs
34 in March – May in India and South Asia peninsula. Driven by the Asian monsoon anticyclone
35 (AMA), the dominant circulation feature in the Indian–Asian upper troposphere–lower stratosphere
36 region during the Asian monsoon, these emissions can be transported to eastern China which
37 contributed to the tropospheric HCN peak in May. The seasonal biomass burning typically occurs

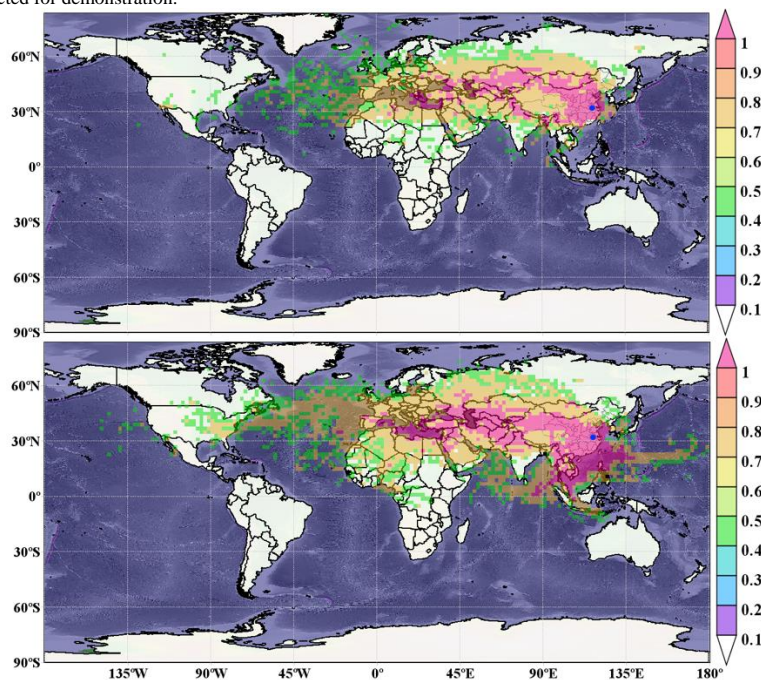


1 in March – May, July – September, and November – December in the eastern part of China. All
2 these emissions can be transported to the observation site at Hefei (32°N) under favorable
3 meteorological condition and thus contribute to all the seasonal tropospheric HCN peaks. The SEAS
4 contribution (mainly China, India and South Asia peninsula) varies over 25 to 80% in March to
5 August.

6 Additionally, a small to moderate portion of wildfire events in central SA, eastern NA, and
7 Northern OCE in autumn or winter could transport to the observation site through long distance
8 atmospheric circulation, which contributed 5 – 20% of the tropospheric HCN in these periods.

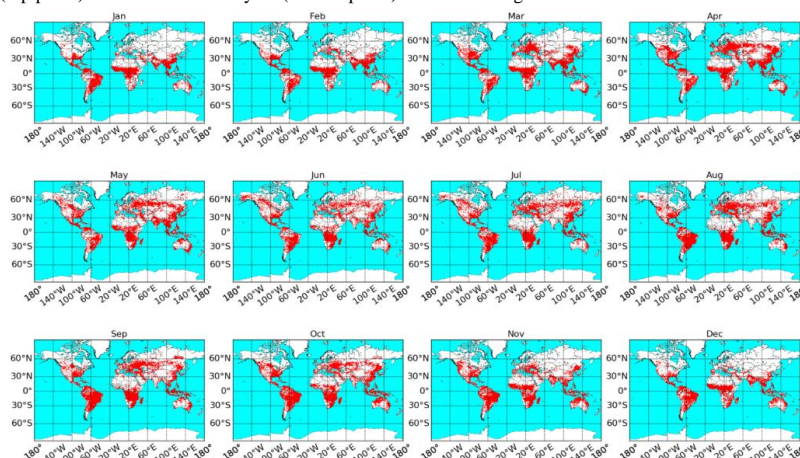


9
10 Fig.11. Travel trajectories of the plumes occurred in AF, SEAS & OCE, EUBA, and NA that reached Hefei (32°N)
11 through long range transport. Travel times are 13, 7, 10, and 14 days, respectively. For clarity, only few trajectories
12 are selected for demonstration.

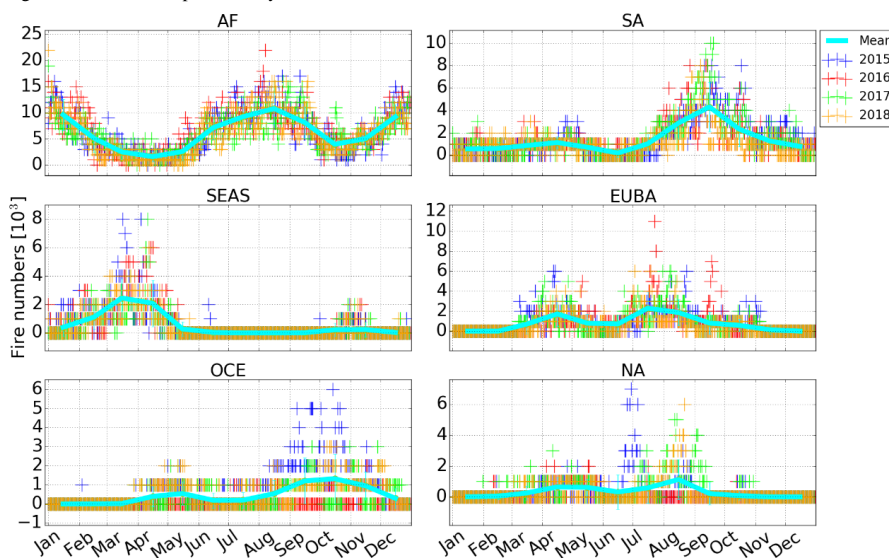




1 Fig.12. Likely source areas of air mass associated with higher HCN concentrations at Hefei (32°N) in the first half
2 year (top panel) and the second half year (bottom panel) identified using PSCF.



3
4 Fig. 13. Global fire map in January to December 2015 accumulated from the FIRMS fire atlas.



5
6 Fig.14. Seasonality of total fire numbers within the AF, SA, SEAS, EUBA, OCE, and NA tracers. All data are
7 accumulated from the FIRMS fire atlas.

8 4.3 Attribution for interannual variability

9 In Fig. 9, the biomass burning contribution was elevated by 5 – 15% between September 2015
10 and July 2016, while no elevations were observed for anthropogenic and oxidation influence. As a
11 result, enhancements of both tropospheric HCN and CO columns between September 2015 and July
12 2016 at Hefei (32°N) were attributed to an elevated influence of biomass burning. In Fig.10, the
13 relative contribution (%) of the SEAS, EUBA, and OCE biomass burning tracers to the total biomass
14 burning associated CO tropospheric column were elevated by 5 – 20%, 8 – 27%, 8 – 31%,
15 respectively, in the second half of 2015 compared to the same period in other years. The relative
16 contribution (%) of the SEAS and OCE biomass burning tracers to the total biomass burning
17 associated CO tropospheric column were elevated by 8 – 39% and 2 – 7%, respectively, in the first
18 half of 2016 compared to the same period in other years.

19 The statistical results of the FIRMS fire atlas data in Fig.14 show that, the fire numbers in the
20 SEAS, EUBA, and OCE regions elevated by 21.89%, 15.72%, and 32.68% between September



1 2015 and July 2016 compared to the same period in other years. These elevated fire numbers in
2 EUBA, SEAS and OCE driven the enhancements of tropospheric HCN and CO columns between
3 September 2015 and July 2016 at Hefei (32°N). Particularly, the number of fires in OCE in the
4 second half of 2015 was greatly elevated in comparison with the other years, acting as a dominant
5 source of tropospheric HCN enhancement in September – December 2015. The fire numbers
6 elevated significantly in the SEAS region in the first half of 2016, which dominated the tropospheric
7 HCN enhancement in January – July 2016.

8 Compared to the northwestern part of China such as the Xinjiang province and the Tibet plateau,
9 the densely populated eastern parts of China are more suitable for crop planting because of fertile
10 soil and adequate water resources. Historically, Chinese farmers burned their crop residue (such as
11 rice, corn, and wheat straws) after harvest to fertilize the soil for the coming farming season. Post-
12 harvest crop residue is a fine fuel that burns directly in the field and mostly by flaming in many
13 mechanized agricultural systems. In contrast, when crops are harvested by hand the residue is often
14 burned in large piles that may smolder for weeks.

15 This seasonal crop residue burning season typically occurs in the spring and summer seasons
16 and also occasionally occurs in the autumn and winter. Pollution gases, dust, and suspended particle
17 matters resulting from crop residue burning emissions result in poor air quality that threaten human
18 health and terrestrial ecosystems. The Chinese presidential decree included the prohibition of crop
19 residue burning into the Law of the People's Republic of China on the Prevention and Control of
20 Atmospheric Pollution in August 2015 (<http://www.chinalaw.gov.cn>, last access on 17 July 2019),
21 and since then the crop residue burning events were banned throughout China. Therefore, we obtain
22 a decrease in fire numbers in China since 2015.

23 In addition, the El Niño Southern Oscillation (ENSO) can cause large scale variations in the
24 convection, circulation, and air temperature of the global atmosphere-ocean system (Liu et al., 2017;
25 Zhao et al., 2002), which could affect the distribution, frequency, and intensity of biomass burning
26 emissions (Schaefer et al., 2018). Furthermore, ENSO could also alter the destruction processes of
27 tropospheric species through their photochemical reactions with tropospheric OH (Zhao et al., 2002).
28 Zeng et al. (2002) found that the abnormally enhancement of tropospheric CO and HCN observed
29 in northern Japan in 1998 were associated with the 1997–1998 ENSO events (Zhao et al., 2002).
30 The large correlation between ENSO and HCN at Lauder (45°S) revealed a detectable ENSO
31 influence on biomass burning (up to 51 % – 55 %) (Schaefer et al., 2018; Zeng et al., 2012).
32 Presumably, the significant enhancements between September 2015 and July 2016 for tropospheric
33 CO and HCN columns at Hefei and most selected NDACC stations were also related to the 2015 –
34 2016 ENSO events.

35 **6 Conclusion**

36 The first multiyear measurements of HCN in the polluted troposphere in densely populated
37 eastern China have been presented here. Tropospheric HCN column amounts were derived from
38 solar spectra recorded with ground-based high spectral resolution Fourier transform infrared (FTIR)
39 spectrometer at Hefei (117°10'E, 31°54'N) between 2015 and 2018. The seasonality and interannual
40 variability of tropospheric HCN columns in eastern China have been investigated. The potential
41 sources that drive the observed HCN seasonality and interannual variability were determined by
42 using the GEOS-Chem tagged CO simulation, the global fire maps and the PSCFs (Potential Source
43 Contribution Function) calculated using HYSPLIT back trajectories.

44 The tropospheric HCN columns over eastern China showed significant seasonal variations with
45 three monthly mean peaks throughout the year. The magnitude of the tropospheric HCN peak in
46 May > September > December. The tropospheric HCN column reached a maximum of (9.8 ± 0.78)
47 $\times 10^{15}$ molecules/cm² in May and a minimum of $(7.16 \pm 0.75) \times 10^{15}$ molecules/cm² in November.
48 In most cases, the tropospheric HCN columns at Hefei (32°N) are higher than the NDACC FTIR
49 observations. Enhancements of the tropospheric HCN columns were observed between September
50 2015 and July 2016 compared to the counterpart measurements in other years. The magnitude of
51 the enhancement ranges from 5 to 46% with an average of 22%. Enhancement of tropospheric HCN
52 (Δ HCN) is correlated with the coincident enhancement of tropospheric CO (Δ CO), indicating that
53 enhancements of tropospheric CO and HCN were due to the same sources.

54 The GEOS-Chem tagged CO simulation, the global fire maps and the PSCFs analysis revealed
55 that the seasonal maxima in May is largely due to the influence of biomass burning in South Eastern
56 Asia (SEAS) ($41 \pm 13.1\%$), Europe and Boreal Asia (EUBA) ($21 \pm 9.3\%$) and Africa (AF) ($22 \pm$
57 4.7%). The seasonal maxima in September is largely due to the influence of biomass burnings in



1 EUBA ($38 \pm 11.3\%$), AF ($26 \pm 6.7\%$), SEAS ($14 \pm 3.3\%$) and NA ($13.8 \pm 8.4\%$). For the seasonal
2 maxima in December, dominant contributions are from AF ($36 \pm 7.1\%$), EUBA ($21 \pm 5.2\%$), and
3 NA ($18.7 \pm 5.2\%$).

4 The enhancements of both tropospheric HCN and CO columns between September 2015 and
5 July 2016 at Hefei (32°N) were attributed to an elevated influence of biomass burnings in SEAS,
6 EUBA, and Oceania (OCE) in this period. Particularly, an elevated fire numbers in OCE in the
7 second half of 2015 dominated the tropospheric HCN enhancement in September – December 2015.
8 An elevated fire numbers in SEAS in the first half of 2016 dominated the tropospheric HCN
9 enhancement in January – July 2016.

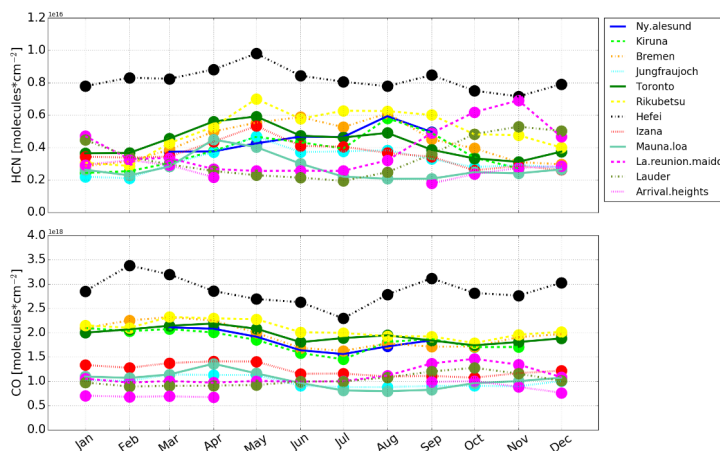
10
11 **Data availability.** The CO and HCN measurements at the selected NDACC sites can be found by
12 the link <http://www.ndaccdemo.org>, and the CO and HCN measurements at Hefei are available on
13 request.

14 **Author contributions.** YS conceived the concept and prepared the paper with inputs from all
15 coauthors. CL, WW, CS, HY, XX, MZ, and JL carried out the experiments. The rest authors
16 contributed to this work via provide refined data or constructive comments.

17 **Competing interests.** The authors declare that they have no conflict of interest.

18 **Acknowledgements.** This work is jointly supported by the National High Technology Research and
19 Development Program of China (No.2019YFC0214800, No.2017YFC0210002, No.
20 2016YFC0203302), the National Science Foundation of China (No. 41605018, No. 41405134,
21 No.41775025, No. 41575021, No. 51778596, No. 91544212, No. 41722501, No. 51778596), and
22 Outstanding Youth Science Foundation (No. 41722501). The processing and post processing
23 environment for SFIT4 are provided by National Center for Atmospheric Research (NCAR),
24 Boulder, Colorado, USA. The NDACC network is acknowledged for supplying the SFIT software
25 and the HCN and CO data. The LINEFIT code is provided by Frank Hase, Karlsruhe Institute of
26 Technology (KIT), Institute for Meteorology and Climate Research (IMK-ASF), Germany. The
27 MeteoInfo software is provided by Prof. Yaqiang Wang, Chinese Academy of Meteorological
28 Sciences. The authors acknowledge the NOAA Air Resources Laboratory (ARL) for making the
29 HYSPLIT transport and dispersion model available on the Internet. The Mauna Loa (20°N) FTIR
30 site is operated by National Center for Atmospheric Research (NCAR), U.S.A., and the Lauder
31 (45°S) and Arrival Heights (78°S) sites are operated by National Institute of Water & Atmospheric
32 Research, New Zealand. The multi-decadal monitoring program of ULiege at the Jungfraujoch
33 station has been primarily supported by the F.R.S.-FNRS and BELSPO (both in Brussels, Belgium)
34 and by the GAW-CH programme of MeteoSwiss. The International Foundation High Altitude
35 Research Stations Jungfraujoch and Gornergrat (HFSJG, Bern) supported the facilities needed to
36 perform the FTIR observations.

37 **Appendix.**



38

39 Fig. A1. Monthly means of the tropospheric CO and HCN columns at Ny Alesund, Kiruna, Bremen, Jungfraujoch,
40 Toronto, Rikubetsu, Hefei, Izana, Mauna Loa, La Reunion Maido, Lauder, and Arrival Heights from 2015 to 2018.



- 1 **References**
- 2 Akagi, S. K., Craven, J. S., Taylor, J. W., McMeeking, G. R., Yokelson, R. J., Burling, I. R., Urbanski, S.
- 3 P., Wold, C. E., Seinfeld, J. H., Coe, H., Alvarado, M. J., and Weise, D. R.: Evolution of trace gases
- 4 and particles emitted by a chaparral fire in California, *Atmospheric Chemistry and Physics*, 12,
- 5 1397-1421, doi:10.5194/acp-12-1397-2012, 2012.
- 6 Ashbaugh, L. L., Malm, W. C., and Sadeh, W. Z.: A residence time probability analysis of sulfur
- 7 concentrations at Grand Canyon National Park, *Atmos. Environ.*, 19, 1263–1270, 1985.
- 8 Akagi, S. K., Yokelson, R. J., Wiedinmyer, C., Alvarado, M. J., Reid, J. S., Karl, T., Crounse, J. D., and
- 9 Wennberg, P. O.: Emission factors for open and domestic biomass burning for use in atmospheric
- 10 models, *Atmospheric Chemistry and Physics*, 11, 4039-4072, doi:10.5194/acp-11-4039-2011, 2011.
- 11 Andreae, M. O. and Merlet, P.: Emission of trace gases and aerosols from biomass burning, *Global*
- 12 *Biogeochemical Cycles*, 15, 955-966, doi:10.1029/2000gb001382, 2001.
- 13 Bange, H. W. and Williams, J.: New Directions: Acetonitrile in atmospheric and biogeochemical cycles,
- 14 *Atmospheric Environment*, 34, 4959-4960, doi:10.1016/s1352-2310(00)00364-2, 2000.
- 15 Bertschi, I., Yokelson, R. J., Ward, D. E., Babbitt, R. E., Susott, R. A., Goode, J. G., and Hao, W. M.:
- 16 Trace gas and particle emissions from fires in large diameter and belowground biomass fuels,
- 17 *Journal of Geophysical Research-Atmospheres*, 108, doi:10.1029/2002jd002100, 2003.
- 18 Barret, B., Mazière, M. D., and Mahieu, E.: Ground-based FTIR measurements of CO from the
- 19 Jungfraujoch: characterisation and comparison with in situ surface and MOPITT data, *Atmospheric*
- 20 *Chemistry and Physics*, 3, 2217–2223, <https://doi.org/10.5194/acp-3-2217-2003>, 2003.
- 21 Chan, K. L.: Biomass burning sources and their contributions to the local air quality in Hong Kong,
- 22 *Science of the Total Environment*, 596, 212-221, doi:10.1016/j.scitotenv.2017.04.091, 2017.
- 23 Chan, K. L., Wiegner, M., Wenig, M., and Poehler, D.: Observations of tropospheric aerosols and NO₂
- 24 in Hong Kong over 5 years using ground based MAX-DOAS, *Science of the Total Environment*,
- 25 619, 1545-1556, doi:10.1016/j.scitotenv.2017.10.153, 2018.
- 26 Dimitriou, K. and Kassomenos, P.: Three year study of tropospheric ozone with back trajectories at a
- 27 metropolitan and a medium scale urban area in Greece, *Sci. Total Environ.*, 502, 493–501, 2015.
- 28 De Maziere, M., Thompson, A. M., Kurylo, M. J., Wild, J. D., Bernhard, G., Blumenstock, T., Braathen,
- 29 G. O., Hannigan, J. W., Lambert, J. C., Leblanc, T., Mcgee, T. J., Nedoluha, G., Petropavlovskikh,
- 30 I., Seckmeyer, G., Simon, P. C., Steinbrecht, W., and Strahan, S. E.: The Network for the Detection
- 31 of Atmospheric Composition Change (NDACC): history, status and perspectives, *Atmospheric*
- 32 *Chemistry and Physics*, 18, 4935-4964, doi:10.5194/acp-18-4935-2018, 2018.
- 33 Freitas, S. R., Longo, K. M., Chatfield, R., Latham, D., Silva Dias, M. A. F., Andreae, M. O., Prins, E.,
- 34 Santos, J. C., Gielow, R., and Carvalho, Jr, J. A.: Including the sub-grid scale plume rise of
- 35 vegetation fires in low resolution atmospheric transport models, *Atmospheric Chemistry and*
- 36 *Physics*, 7, 3385–3398, 2007.
- 37 Fisher, J. A., Murray, L., Jones, D. B. A., and Deutscher, N. M.: Improved method for linear carbon
- 38 monoxide simulation and source attribution in atmospheric chemistry models illustrated using
- 39 GEOS-Chem v9, *Geophysical Model Development*, 10, 4129–4144, [https://doi.org/10.5194/gmd-](https://doi.org/10.5194/gmd-10-4129-2017)
- 40 [10-4129-2017](https://doi.org/10.5194/gmd-10-4129-2017), 2017.
- 41 Giglio, L., Randerson, J. T., and van der Werf, G. R.: Analysis of daily, monthly, and annual burned area
- 42 using the fourth-generation global fire emissions database (GFED4), *Journal of Geophysical*
- 43 *Research: Biogeosciences*, 118, 317–328, <https://doi.org/10.1002/jgrg.20042>, 2013.
- 44 Guenther, A. B., Jiang, X., Heald, C. L., Sakulyanontvittaya, T., Duhl, T., Emmons, L. K., and Wang, X.:
- 45 The Model of Emissions of Gases and Aerosols from Nature version 2.1 (MEGAN2.1): An extended
- 46 and updated framework for modeling biogenic emissions, *Geoscientific Model Development*, 5,
- 47 1471–1492, <https://doi.org/10.5194/gmd-5-1471-2012>, 2012.
- 48 Giuseppe, F. D., Rémy, S., Pappenberger, F., and Wetterhall, F.: Using the Fire Weather Index (FWI) to
- 49 improve the estimation of fire emissions from fire radiative power (FRP) observations, *Atmospheric*
- 50 *Chemistry and Physics*, 18, 5359–5370, <https://doi.org/10.5194/acp-18-5359-2018>, 2018.
- 51 Hase, F., Hannigan, J. W., Coffey, M. T., Goldman, A., Höpfner, M., Jones, N. B., Rinsland, C. P., and
- 52 Wood, S. W.: Intercomparison of retrieval codes used for the analysis of high-resolution, ground-
- 53 based FTIR measurements, *J. Quant. Spectrosc. Ra.*, 87, 25–52, 2004.
- 54 Hase, F.: Improved instrumental line shape monitoring for the ground-based, high-resolution FTIR
- 55 spectrometers of the Network for the Detection of Atmospheric Composition Change, *Atmospheric*
- 56 *Measurement Techniques*, 5, 603-610, doi:10.5194/amt-5-603-2012, 2012.
- 57 Holzinger, R., Warneke, C., Hansel, A., Jordan, A., Lindinger, W., Scharffe, D. H., Schade, G., and
- 58 Crutzen, P. J.: Biomass burning as a source of formaldehyde, acetaldehyde, methanol, acetone,
- 59 acetonitrile, and hydrogen cyanide, *Geophysical Research Letters*, 26, 1161-
- 60 1164, doi:10.1029/1999gl900156, 1999.



- 1 Holtslag, A. A. M. and Boville, B. A.: Local Versus Nonlocal Boundary-Layer Diffusion in a Global
2 Climate Model, *Journal of Climate*, 6, 1825–1842, <https://doi.org/10.1175/1520->
3 0442(1993)006<1825:LVNBLD>2.0.CO;2, 1993.
- 4 Kaiser, J. W., Heil, A., Andreae, M. O., Benedetti, A., Chubarova, N., Jones, L., Morcrette, J.-J., Razinger,
5 M., Schultz, M. G., Suttie, M., and van der Werf, G. R.: Biomass burning emissions estimated with
6 a global fire assimilation system based on observed fire radiative power, *Biogeosciences*, 9, 527–
7 554, <https://doi.org/10.5194/bg-9-527-2012>, 2012.
- 8 Kaiser, A., Scheifinger, H., Spangl, W., Weiss, A., Gilge, S., Fricke, W., Ries, L., Cemas, D., and
9 Jesenovec, B.: Transport of nitrogen oxides, carbon monoxide and ozone to the alpine global
10 atmosphere watch stations Jungfraujoch (Switzerland), Zugspitze and Hohenpeißenberg (Germany),
11 *Sonnblick (Austria) and Mt.Krvavec (Slovenia)*, *Atmos. Environ.*, 41, 9273–9287, 2007.
- 12 Hoesly R. M., Smith S. J., Feng L. Y., Klimont Z., Janssens-Maenhout G., Pitkanen T., Seibert J. J., Vu
13 L., Andres R. J., Bolt R. M., Bond T. C., Dawidowski L., Kholod N., Kurokawa J., Li M., Liu L.,
14 Lu Z. F., Moura M. C. P., O'Rourke P. R., and Zhang Q., "Historical (1750-2014) anthropogenic
15 emissions of reactive gases and aerosols from the Community Emissions Data System (CEDS)," *Geosci. Model Dev.* 11, 369-408 (2018).
- 16 Li, Q., Palmer, P. I., Pumphrey, H. C., Bernath, P., and Mahieu, E.: What drives the observed variability
17 of HCN in the troposphere and lower stratosphere?, *Atmospheric Chemistry and Physics*, 9, 8531-
18 8543, doi:10.5194/acp-9-8531-2009, 2009.
- 19 Li, Q. B., Jacob, D. J., Bey, I., Yantosca, R. M., Zhao, Y. J., Kondo, Y., and Notholt, J.: Atmospheric
20 hydrogen cyanide (HCN): Biomass burning source, ocean sink?, *Geophysical Research Letters*, 27,
21 357-360, doi:10.1029/1999gl010935, 2000.
- 22 Li, Q. B., Jacob, D. J., Yantosca, R. M., Heald, C. L., Singh, H. B., Koike, M., Zhao, Y. J., Sachse, G.
23 W., and Streets, D. G.: A global three-dimensional model analysis of the atmospheric budgets of
24 HCN and CH₃CN: Constraints from aircraft and ground measurements, *Journal of Geophysical*
25 *Research-Atmospheres*, 108, doi:10.1029/2002jd003075, 2003.
- 26 Li M., Zhang Q., Kurokawa J., Woo J. H., He K. B., Lu Z. F., Ohara T., Song Y., Streets D. G., Carmichael
27 G. R., Cheng Y. F., Hong C. P., Huo H., Jiang X. J., Kang S. C., Liu F., Su H., and Zheng B., "MIX:
28 a mosaic Asian anthropogenic emission inventory under the international collaboration framework
29 of the MICS-Asia and HTAP," *Atmos Chem Phys* 17, 935-963 (2017).
- 30 Liu, Y., Cobb, K. M., Song, H. M., Li, Q., Li, C. Y., Nakatsuka, T., An, Z. S., Zhou, W. J., Cai, Q. F., Li,
31 J. B., Leavitt, S. W., Sun, C. F., Mei, R. C., Shen, C. C., Chan, M. H., Sun, J. Y., Yan, L. B., Lei, Y.,
32 Ma, Y. Y., Li, X. X., Chen, D. L., and Linderholm, H. W.: Recent enhancement of central Pacific El
33 Nino variability relative to last eight centuries, *Nature Communications*, 8, doi:ARTN
34 1538610.1038/ncomms15386, 2017.
- 35 Lobert, J. M., Scharffe, D. H., Hao, W. M., and Crutzen, P. J.: Importance of biomass burning in the
36 atmospheric budgets of nitrogen-containing gases, *Nature*, 346, 552-554, doi:10.1038/346552a0,
37 1990.
- 38 Lupu, A., Kaminski, J. W., Neary, L., McConnell, J. C., Toyota, K., Rinsland, C. P., Bernath, P. F., Walker,
39 K. A., Boone, C. D., Nagahama, Y., and Suzuki, K.: Hydrogen cyanide in the upper troposphere:
40 GEM-AQ simulation and comparison with ACE-FTS observations, *Atmospheric Chemistry and*
41 *Physics*, 9, 4301-4313, doi:10.5194/acp-9-4301-2009, 2009.
- 42 Lutsch, E., Dammers, E., Conway, S., and Strong, K.: Long-range transport of NH₃, CO, HCN, and C₂H₆
43 from the 2014 Canadian Wildfires, *Geophysical Research Letters*, 43, 8286-
44 8297, doi:10.1002/2016gl070114, 2016.
- 45 Mahieu, E., Zander, R., Delbouille, L., Demoulin, P., Roland, G., and Servais, C.: Observed trends in
46 total vertical column abundances of atmospheric gases from IR solar spectra recorded at the
47 Jungfraujoch, *Journal of Atmospheric Chemistry*, 28, 227-243, doi:10.1023/a:1005854926740,
48 1997.
- 49 Nagahama, Y. and Suzuki, K.: The influence of forest fires on CO, HCN, C₂H₆, and C₂H₂ over northern
50 Japan measured by infrared solar spectroscopy, *Atmospheric Environment*, 41, 9570-
51 9579, doi:10.1016/j.atmosenv.2007.08.043, 2007.
- 52 Notholt, J., Toon, G. C., Rinsland, C. P., Pougatchev, N. S., Jones, N. B., Connor, B. J., Weller, R.,
53 Gautrois, M., and Schrems, O.: Latitudinal variations of trace gas concentrations in the free
54 troposphere measured by solar absorption spectroscopy during a ship cruise, *Journal of Geophysical*
55 *Research-Atmospheres*, 105, 1337-1349, doi:10.1029/1999jd900940, 2000.
- 56 Patra, P. K., Houweling, S., Krol, M., Bousquet, P., Belikov, D., Bergmann, D., Bian, H., Cameron-Smith,
57 P., Chipperfield, M. P., Corbin, K., Fortems-Cheiney, A., Fraser, A., Gloor, E., Hess, P., Ito, A., Kawa,
58 S. R., Law, R. M., Loh, Z., Maksyutov, S., Meng, L., Palmer, P. I., Prinn, R. G., Rigby, M., Saito, R.,
59 and Wilson, C.: TransCom model simulations of CH₄ and related species: Linking transport, surface
60



- 1 flux and chemical loss with CH₄ variability in the troposphere and lower stratosphere, *Atmospheric*
2 *Chemistry and Physics*, 11, 12 813–12 837, <https://doi.org/10.5194/acp-11-12813-2011>, 2011.
- 3 Polissar, A., Hopke, P., Paatero, P., Kaufmann, Y., Hall, D., Bodhaine, B., Dutton, E., and Harris, J.: The
4 aerosol at Barrow, Alaska: long-term trends and source locations, *Atmos. Environ.*, 33, 2441–2458,
5 1999.
- 6 Rinsland, C. P., Dufour, G., Boone, C. D., Bernath, P. F., Chiou, L., Coheur, P. F., Turquety, S., and
7 Clerbaux, C.: Satellite boreal measurements over Alaska and Canada during June–July 2004:
8 Simultaneous measurements of upper tropospheric CO, C₂H₆, HCN, CH₃Cl, CH₄, C₂H₂, CH₃OH,
9 HCOOH, OCS, and SF₆ mixing ratios, *Global Biogeochemical Cycles*, 21, doi:Artn Gb3008
10 10.1029/2006gb002795, 2007.
- 11 Rinsland, C. P., Jones, N. B., Connor, B. J., Wood, S. W., Goldman, A., Stephen, T. M., Murcray, F. J.,
12 Chiou, L. S., Zander, R., and Mahieu, E.: Multiyear infrared solar spectroscopic measurements of
13 HCN, CO, C₂H₆, and C₂H₂ tropospheric columns above Lauder, New Zealand (45 degrees S latitude),
14 *Journal of Geophysical Research-Atmospheres*, 107, doi:Artn 418510.1029/2001jd001150, 2002.
- 15 Rodgers, C. D.: *Inverse Methods for Atmospheric Sounding: Theory and Practice*, Singapore, 2000.
- 16 Rodgers, C. D. and Connor, B. J.: Intercomparison of remote sounding instruments, *Journal of*
17 *Geophysical Research: Atmospheres*, 108, 4116, <https://doi.org/10.1029/2002JD002299>, 2003.
- 18 Rothman, L. S., Gordon, I. E., Barbe, A., Benner, D. C., Bernath, P. E., Birk, M., Boudon, V., Brown, L.
19 R., Campargue, A., Champion, J. P., Chance, K., Coudert, L. H., Dana, V., Devi, V. M., Fally, S.,
20 Flaud, J. M., Gamache, R. R., Goldman, A., Jacquemart, D., Kleiner, I., Lacombe, N., Lafferty, W.
21 J., Mandin, J. Y., Massie, S. T., Mikhailenko, S. N., Miller, C. E., Moazzen-Ahmadi, N., Naumenko,
22 O. V., Nikitin, A. V., Orphal, J., Perevalov, V. I., Perrin, A., Predoi-Cross, A., Rinsland, C. P., Rotger,
23 M., Simeckova, M., Smith, M. A. H., Sung, K., Tashkun, S. A., Tennyson, J., Toth, R. A., Vandaele,
24 A. C., and Vander Auwera, J.: The HITRAN 2008 molecular spectroscopic database, *Journal of*
25 *Quantitative Spectroscopy & Radiative Transfer*, 110, 533–572, doi:10.1016/j.jqsrt.2009.02.013,
26 2009.
- 27 Rémy, S., Veira, A., Paugam, R., Sofiev, M., Kaiser, J. W., Marengo, F., Burton, S. P., Benedetti, A.,
28 Engelen, R. J., Ferrare, R., and Hair, J. W.: Two global data sets of daily fire emission injection
29 heights since 2003, *Atmospheric Chemistry and Physics*, 17, 2921–2942,
30 <https://doi.org/10.5194/acp-17-2921-2017>, 2017.
- 31 Spivakovsky, C. M., Logan, J. A., Montzka, S. A., Balkanski, Y. J., Foreman-Fowler, M., Jones, D. B.
32 A., Horowitz, L. W., Fusco, A. C., Brenninkmeijer, C. A. M., Prather, M. J., Wofsy, S. C., and
33 McElroy, M. B.: Three-dimensional climatological distribution of tropospheric OH: Update and
34 evaluation, *Journal of Geophysical Research: Atmospheres*, 105, 8931–8980,
35 <https://doi.org/10.1029/1999JD901006>, 2000.
- 36 Sofiev, M., Ermakova, T., and Vankevich, R.: Evaluation of the smoke-injection height from wild-land
37 fires using remote-sensing data, *Atmospheric Chemistry and Physics*, 12, 1995–2006,
38 <https://doi.org/10.5194/acp-12-1995-2012>, 2012.
- 39 Shindell, D. T., Faluvegi, G., Stevenson, D. S., Krol, M. C., Emmons, L. K., Lamarque, J.-F., Pétron, G.,
40 Dentener, F. J., Ellingsen, K., Schultz, M. G., Wild, O., Amann, M., Atherton, C. S., Bergmann, D.
41 J., Bey, I., Butler, T., Cofala, J., Collins, W. J., Derwent, R. G., Doherty, R. M., Drevet, J., Eskes, H.
42 J., Fiore, A. M., Gauss, M., Hauglustaine, D. A., Horowitz, L. W., Isaksen, I. S. A., Lawrence, M.
43 G., Montanaro, V., Müller, J.-F., Pitari, G., Prather, M. J., Pyle, J. A., Rast, S., Rodriguez, J. M.,
44 Sanderson, M. G., Savage, N. H., Strahan, S. E., Sudo, K., Szopa, S., Unger, N., van Noije, T. P. C.,
45 and Zeng, G.: Multimodel simulations of carbon monoxide: Comparison with observations and
46 projected near-future changes, *Journal of Geophysical Research: Atmospheres*, 111, L01 104,
47 <https://doi.org/10.1029/2006JD007100>, 2006.
- 48 Schaefer, H., Smale, D., Nichol, S. E., Bromley, T. M., Brailsford, G. W., Martin, R. J., Moss, R., Englund
49 Michel, S., and White, J. W. C.: Limited impact of El Niño–Southern Oscillation on variability and
50 growth rate of atmospheric methane, *Biogeosciences*, 15, 6371–6386, doi:10.5194/bg-15-6371-2018,
51 2018.
- 52 Sun, Y. W., Liu, C., Palm, M., Vigouroux, C., Notholt, J., Hui, Q. H., Jones, N., Wang, W., Su, W. J.,
53 Zhang, W. Q., Shan, C. G., Tian, Y., Xu, X. W., De Maziere, M., Zhou, M. Q., and Liu, J. G.: Ozone
54 seasonal evolution and photochemical production regime in the polluted troposphere in eastern
55 China derived from high-resolution Fourier transform spectrometry (FTS) observations,
56 *Atmospheric Chemistry and Physics*, 18, 14569–14583, doi:10.5194/acp-18-14569-2018, 2018a.
- 57 Sun, Y. W., Palm, M., Liu, C., Hase, F., Griffith, D., Weinzierl, C., Petri, C., Wang, W., and Notholt, J.:
58 The influence of instrumental line shape degradation on NDACC gas retrievals: total column and
59 profile, *Atmospheric Measurement Techniques*, 11, 2879–2896, doi:10.5194/amt-11-2879-2018,
60 2018b.



- 1 Tang, G., Wang, Y., Li, X., Ji, D., Hsu, S., and Gao, X.: Spatial-temporal variations in surface ozone in
2 Northern China as observed during 2009–2010 and possible implications for future air quality
3 control strategies, *Atmos. Chem. Phys.*, 12, 2757–2776, doi:10.5194/acp-12-2757-2012, 2012.
- 4 Tian, Y., Sun, Y., Liu, C., Wang, W., Shan, C., Xu, X., and Hu, Q.: Characterisation of methane variability
5 and trends from near-infrared solar spectra over Hefei, China, *Atmospheric Environment*,
6 173, doi:10.1016/j.atmosenv.2017.11.001, 2017.
- 7 Viatte, C., Strong, K., Hannigan, J., Nussbaumer, E., Emmons, L. K., Conway, S., Paton-Walsh, C.,
8 Hartley, J., Benmergui, J., and Lin, J.: Identifying fire plumes in the Arctic with tropospheric FTIR
9 measurements and transport models, *Atmospheric Chemistry and Physics*, 15, 2227–
10 2246, doi:10.5194/acp-15-2227-2015, 2015.
- 11 Viatte, C., Strong, K., Walker, K. A., and Drummond, J. R.: Five years of CO, HCN, C₂H₆, C₂H₂, CH₃OH,
12 HCOOH and H₂CO total columns measured in the Canadian high Arctic, *Atmospheric*
13 *Measurement Techniques*, 7, 1547–1570, doi:10.5194/amt-7-1547-2014, 2014.
- 14 Vigouroux, C., Stavrakou, T., Whaley, C., Dils, B., Duflot, V., Hermans, C., Kumps, N., Metzger, J. M.,
15 Scolas, F., Vanhaelewyn, G., Muller, J. F., Jones, D. B. A., Li, Q., and De Maziere, M.: FTIR time-
16 series of biomass burning products (HCN, C₂H₆, C₂H₂, CH₃OH, and HCOOH) at Reunion Island
17 (21 degrees S, 55 degrees E) and comparisons with model data, *Atmospheric Chemistry and Physics*,
18 12, 10367–10385, doi:10.5194/acp-12-10367-2012, 2012.
- 19 Wang, T., Xue, L. K., Brimblecombe, P., Lam, Y. F., Li, L., and Zhang, L.: Ozone pollution in China: A
20 review of concentrations, meteorological influences, chemical precursors, and effects, *Science of*
21 *the Total Environment*, 575, 1582–1596, doi:10.1016/j.scitotenv.2016.10.081, 2017.
- 22 Xiaoyan, W., Huixiang, W., and Shaoli, W.: Ambient formaldehyde and its contributing factor to ozone
23 and OH radical in a rural area, *Atmospheric Environment*, 44, 2074–
24 2078, doi:https://doi.org/10.1016/j.atmosenv.2010.03.023, 2010.
- 25 Xing, C., Liu, C., Wang, S., Chan, K. L., Gao, Y., Huang, X., Su, W., Zhang, C., Dong, Y., Fan, G., Zhang,
26 T., Chen, Z., Hu, Q., Su, H., Xie, Z., and Liu, J.: Observations of the vertical distributions of
27 summertime atmospheric pollutants and the corresponding ozone production in Shanghai, China,
28 *Atmos. Chem. Phys.*, 17, 14275–14289, doi:10.5194/acp-17-14275-2017, 2017.
- 29 Yevich, R. and Logan, J. A.: An assessment of biofuel use and burning of agricultural waste in the
30 developing world, *Global Biogeochemical Cycles*, 17, 1095,
31 https://doi.org/10.1029/2002GB001952, 2003.
- 32 Yokelson, R. J., Susott, R., Ward, D. E., Reardon, J., and Griffith, D. W. T.: Emissions from smoldering
33 combustion of biomass measured by open-path Fourier transform infrared spectroscopy, *Journal of*
34 *Geophysical Research-Atmospheres*, 102, 18865–18877, doi:10.1029/97jd00852, 1997.
- 35 York, D., Evensen, N. M., Martinez, M. L., and Delgado, J. D.: Unified equations for the slope, intercept,
36 and standard errors of the best straight line, *American Journal of Physics*, 72, 367–
37 375, doi:10.1119/1.1632486, 2004.
- 38 Yin, X., Kang, S., de Foy, B., Cong, Z., Luo, J., Zhang, L., Ma, Y., Zhang, G., Rupakheti, D., and Zhang,
39 Q.: Surface ozone at Nam Co in the inland Tibetan Plateau: variation, synthesis comparison and
40 regional representativeness, *Atmos. Chem. Phys.*, 17, 11293–11311, https://doi.org/10.5194/acp-
41 17-11293-2017, 2017.
- 42 Zeng, G., Wood, S. W., Morgenstern, O., Jones, N. B., Robinson, J., and Smale, D.: Trends and variations
43 in CO, C₂H₆, and HCN in the Southern Hemisphere point to the declining anthropogenic emissions
44 of CO and C₂H₆, *Atmospheric Chemistry and Physics*, 12, 7543–7555, doi:10.5194/acp-12-7543-
45 2012, 2012.
- 46 Zhao, Y., Kondo, Y., Murcray, F. J., Liu, X., Koike, M., Irie, H., Strong, K., Suzuki, K., Sera, M., and
47 Ikegami, Y.: Seasonal variations of HCN over northern Japan measured by ground-based infrared
48 solar spectroscopy, *Geophysical Research Letters*, 27, 2085–2088, doi:10.1029/1999gl1011218,
49 2000.
- 50 Zhao, Y., Strong, K., Kondo, Y., Koike, M., Matsumi, Y., Irie, H., Rinsland, C. P., Jones, N. B., Suzuki,
51 K., Nakajima, H., Nakane, H., and Murata, I.: Spectroscopic measurements of tropospheric CO,
52 C₂H₆, C₂H₂, and HCN in northern Japan, *Journal of Geophysical Research-Atmospheres*,
53 107, doi:10.1029/2001jd000748, 2002.